Western University

Scholarship@Western

Digitized Theses

Digitized Special Collections

2008

Design of a Transceive Coil Array for Parallel Imaging at 9.4T

Samuel Oluwagbemiga Oduneye
Western University

Follow this and additional works at: https://ir.lib.uwo.ca/digitizedtheses

Recommended Citation

Oduneye, Samuel Oluwagbemiga, "Design of a Transceive Coil Array for Parallel Imaging at 9.4T" (2008). *Digitized Theses*. 4145.
https://ir.lib.uwo.ca/digitizedtheses/4145

This Thesis is brought to you for free and open access by the Digitized Special Collections at Scholarship@Western. It has been accepted for inclusion in Digitized Theses by an authorized administrator of Scholarship@Western. For more information, please contact wlswadmin@uwo.ca.

Design of a Transceive Coil Array for Parallel Imaging at 9.4T

(Spine title: Design of a Transceive Coil Array)
(Thesis format: Monograph)

by

Samuel Oluwagbemiga Oduneye

Graduate Program In Biomedical Engineering

Submitted in partial fulfillment
of the requirements for the degree of
Master of Engineering Science

School of Graduate and Postdoctoral Studies
The University of Western Ontario
London, Ontario, Canada

December 8, 2008

© Samuel O. Oduneye, 2008

THE UNIVERSITY OF WESTERN ONTARIO
SCHOOL OF GRADUATE AND POSTDOCTORAL STUDIES

CERTIFICATE OF EXAMINATION

Chief Advisor	**Examining Board**
Dr. Ravi S. Menon	Dr. Charles McKenzie
Advisory Committee	Dr. Terry Peters
Dr. Rob Bartha	Dr. Paula Foster
Dr. Brian K. Rutt	

The thesis by

Samuel O. Oduneye

entitled

Design of a Transceive Coil Array for Parallel Imaging at 9.4T

is accepted in partial fulfillment of the
requirements for the degree of
Masters of Engineering Science

Chair of Examination Board

Dated this 8th day of December, 2008.

Dr. Jim Johnson

Abstract

The main goal of this thesis is to design and develop a transmit/receive (transceive) coil array for small animal imaging at 9.4T. The goal is achieved by following basic RF design principles with a methodical construction approach and demonstrating viable applications.

As operational frequencies increase linearly with higher static fields, the wavelength approaches the size of the sample being imaged. The resulting standing wave mode deteriorates image homogeneity. Fortunately, with multi-channel coil arrays, the produced B_1 field can be tailored to produce a homogeneous excitation in the region of interest, thus overcoming the so called dielectric resonance effect. We examined a solution to achieve a higher level of B_1 homogeneity and we compared the improvement of RF wavelength effects reduction against the results obtained with a similar-sized conventional birdcage coil.

An additional benefit of this design lies in the fact that the use of multiple receiving coil elements is necessary for the implementation of fast imaging acquisition techniques such as parallel imaging. This is possible because the distinct element sensitivities are used to reconstruct conventional images from undersampled (or accelerated) data. The greatest advantage of parallel imaging is thus the reduction of total acquisition time.

In functional MRI (fMRI), single-shot EPI is one of the standard imaging technique. Unfortunately, EPI suffers from significant limitations, precisely because all of the data is acquired following a single RF excitation. As a result EPI images can manifest artifacts and blurring due to susceptibility mismatch, off-resonance effects and reduced signal at the edges of k-space. Fortunately, parallel imaging can be used to decrease such unwanted effects by reducing the total k-space data acquired. Presented in this thesis is the logical progression of the construction of a transceive coil from surface coil fundamentals to high field applications such as field focusing and parallel imaging techniques.

Key words: Magnetic Resonance Imaging (MRI), RF Engineering, Small Animal Imaging, Phased Array, Surface Coil, Electromagnetic Field Coupling, Parallel Imaging, Sensitivity Encoding (SENSE), Generalized Autocalibrating Partially Parallel Acquisition (GRAPPA), Head Imaging, Echo Planar Imaging (EPI), function MRI (fMRI), Fast Image acquisition, Artifacts.

... *In the midst of darkness light persists* ...

by Martin Luther King

(and before him Mahatma Gandhi)

Dedicated to

my parents who offered unconditional love and support throughout my studies

Acknowledgments

Whether you call it divine providence, destiny or chance as I approach the end of this chapter of my life, I can only look back and appreciate the greatness of all of the events that led me to this moment and most important thank the host of people that have crossed my path and made a contribution. As I am extremely excited for what lies ahead, I am forever grateful to all of you.

I would like to thank my supervisor, Dr. Ravi Menon, for challenging me over the past two years and teaching me the importance of accurate knowledge reporting in science. Significant guidance was also provided by the members of the advisory committee: Dr. Rob Bartha and Dr. Brian Rutt. Your suggestions undoubtedly steered me into the right direction.

Special thanks go to Dr. Robert Pinkerton, Dr. Craig Jones, Dr. Martyn Klassen and Dr. Charles McKenzie for helpful discussions and recommendations, Jeff Mason for his technical support, the rest of the lab members and Diana Timmermans for being an incredible program administrator, going above and beyond her job description.

To my "board of advisors" from Ryerson University, Robarts and UWO from whom I've always sought advice, Dr. Mike Kassam, Dr. Gosha Zywno, Dr. Jayshri Sabarinathan. Whether you know it or not your mentorship and support is and will always be extremely valuable to me.

A dearest thank goes to my family and friends, for caring and been always there for me. Last but not least, I would like to thank Onye Nnorom. She has been my rock throughout this incredible roller coaster that these past two years have been. Without her unconditional support and love I would have lost my sanity and serenity somewhere along the way. Change her and I am changed also. I look forward to many more exciting years together.

Contents

List of Figures

List of Acronyms & Abbreviations

ACS	Auto Calibration Signal
DAM	Double Angle Method
EMF	Electromotive Force
EPI	Echo Planar Imaging
ETL	Echo Train Length
FD	Frequency Diameter
FID	Free Induction Decay
FLASH	Fast Low Angle Shot
FOV	Field Of View
FSE	Fast Spin Echo
GRAPPA	Generalized Auto Calibrating Partially Parallel Acquisition
MRI	Magnetic Resonance Imaging
PI	Parallel Imaging
RF	Radio Frequency
RMS	Root Mean Square
ROI	Region Of Interest
SENSE	Sensitivity Encoding
SMASH	Simultaneous Acquisition Of Spatial Harmonics
SNR	Signal To Noise Ratio
SOS	Sum Of Squares

Preface

Radio Frequency (RF) coils are integral components of a Magnetic Resonance Imaging (MRI) system, as they are required to excite nuclear spins and then capture the electromagnetic signals from the excited spins. For this reason, RF coils need to satisfy specific requirements: transmit coils must produce an RF magnetic field with high homogeneity over the region of interest, receive coils must ensure uniformity of the RF receive response over the largest possible sample volume and must have high signal-to-noise ratio (SNR). The desire to achieve higher SNR in MR images has given rise to scanner construction with increasingly higher static magnetic field by the manufacturers. Unfortunately, higher fields induce a drastic change in the RF behavior, posing constant challenges to the design and construction of RF coils. Specifically, as operational frequencies increase linearly with static field strength, the signal wavelength decreases, becoming comparable in size to the sample dimensions. The result is unwanted RF wave effects, that are easily observable in MR images in the form of localized high signal intensity in center regions and low signal intensity in peripheral regions. Although traditional volume coil designs, such as the birdcage coil are highly reliable, in ultra-high field imaging RF wavelength phenomena have been observed in images acquired with such coils. An alternative design, transceive array coils are designed to be used in both transmit and receive operation. For transmission, the elements of the multiple array coil can be controlled individually to tailor the induced B_1 field and to overcome the RF induced artifacts, for reception each coil element can use its sensitivity for fast spatial encoding operation such as parallel imaging. Parallel imaging exploits the difference in sensitivities between individual coil elements in a receive array to reduce the number of gradient encoding steps required for imaging, thus reducing the overall acquisition time. While these are significant advantages, the construction of a multi-coil array coil is far from trivial and requires systematic and rigorous attention to achieve optimal performance. The research focused on three main objectives. First, to develop a transmit-receive RF coil for small animal imaging. This coil would operate in an environment where bore space is limited, hence justifying the elimination of a body coil. Second, to produce a transmit field (B_1^+) that can compensate for RF wavelength effects. Finally, to use spatially varying sensitivity information to implement parallel imaging acquisition with the same coil.

Chapter 1

Principles Of Magnetic Resonance Imaging

1.1 Introduction

1.1.1 Historical Facts

The Nuclear Magnetic Resonance (NMR) phenomenon was formalized in the 1930s by Isidor Isaac Rabi and later independently refined (1946) by Felix Bloch and Edward Purcell [1, 2], for which they shared a Noble prize in 1952. NMR was used predominantly in physics, biochemistry and analytical chemistry. Not until 1973, did Lauterbur report the first MR images using linear gradient fields and the back projection reconstruction technique [3]. The 1970s and 1980s saw increase in MR investments by the industry and hospitals, which realized that it was necessary to spend large amounts of money for medical imaging hardware advancement.

1.1.2 Magnetic Resonance Classical Description

Atoms with an odd number of protons exhibit an MR phenomenon attributed to the nuclear spin angular momentum. In classical physics, these nuclei are represented

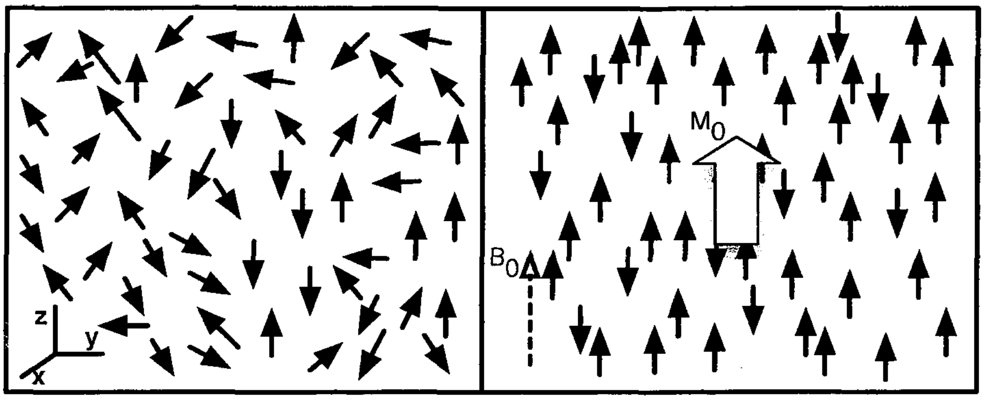

Fig. 1.1: Equilibrium status after magnetization is exposed to static magnetic field B_0

as spinning charged spheres along an axis and often referred to as *spins.* Atoms such as ^{1}H, ^{31}P and ^{23}Na exhibit this MR phenomenon, however ^{1}H is the most abundant in biological systems and also the most sensitive. Therefore, imaging based on ^{1}H is the most studied. (For the remainder of this thesis I will refer to the water proton ^{1}H in H_2O, unless otherwise specified).

As shown in Fig. 1.1, in the absence of an external magnetic field, the spins are randomly aligned, however in the presence of an external magnetic field $\overrightarrow{B_0}$, a magnetization moment $\overrightarrow{M}$ is produced in the direction of $\overrightarrow{B_0}$. This magnetization can be defined as the addition of all the magnetic moments per unit volume, $\overrightarrow{M} = \sum \overrightarrow{\mu}$, and its potential energy E is then defined by

$$E = -\overrightarrow{\mu} \cdot \overrightarrow{B_0}. \tag{1.1}$$

Because hydrogen has two different spin operators (the proton has a spin number of $\frac{1}{2}$), it can be found in one of two spins states where $+\frac{1}{2}$ is spin up or -$\frac{1}{2}$ is spin down. This proton characteristic leads to two energy states separated by

$$\Delta E = h\frac{\gamma}{2\pi}B_0 \tag{1.2}$$

where h is Plancks constant, γ is the gyromagnetic ratio and B_0 the magnetic field.

The energy difference in Eqn. 1.2 gives rise to two nuclei populations: one parallel (spin up, n_+) and one anti-parallel (spin down, n_-). In Fig. 1.2, the quantized energy levels are shown. Even though the natural tendency of the spins is to align with the magnetic field and occupy the minimum energy state, thermal energy is sufficient to exceed the energy separation and place some spins in the higher energy state. Therefore, the ratio of the number of spins depends on the Boltzmann's distribution:

$$\frac{n_-}{n_+} = e^{-\Delta E/kT} \tag{1.3}$$

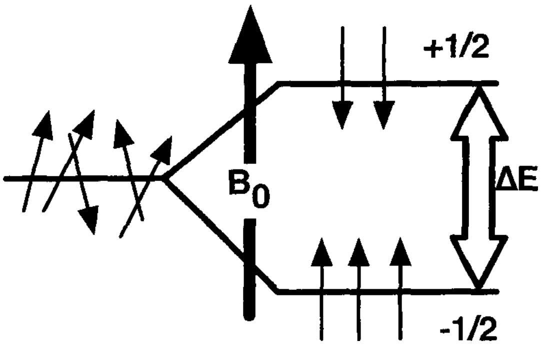

Fig. 1.2: Zeeman diagram. On the left the energy state in absence of an external magnetic field and on the right the split into energy levels when a field B_0 is applied. The difference in energy ΔE is proportional to the size of B_0

where k is the Boltzmann's constant and T is absolute temperature. Usually, this ratio indicates that only 5-7 ppm of spins are in the parallel state, and even if the difference may appear very small, this excess accounts for the polarization of the magnetization vector. The equilibrium magnetization vector for protons can be expressed in the following manner

$$M_0 = \rho_0 \frac{\gamma^2 \hbar^2}{4kT} B_0 \tag{1.4}$$

where ρ_0 is the proton spin density and $\hbar$ is defined as $h/2\pi$. In addition, the energy difference expressed is Eqn. 1.2 is related to the photon energy by $E = h \cdot f$, where f is the photon's precession frequency. Therefore, only the electromagnetic field operating at that frequency is able to excite the spins between states. When a spin makes a transition from a higher to a lower energy state, a photon of ΔE energy is emitted. Thus, the transmit frequency to excite the spins is the same frequency required to receive the MR signal. The spins resonate at a well-defined resonance frequency, known as the $Larmor frequency$. The Larmor frequency is related to the magnetic field as shown in Eqn. 1.5 and Eqn. 1.6

$$\omega = \gamma B_0 \tag{1.5}$$

$$f = \frac{\gamma}{2\pi} B_0. \tag{1.6}$$

The Larmor frequency is one of the most important relationships in MRI, linking resonance frequency to magnetic field. The gyromagnetic ratio (γ) is a property of the nucleus being examined. Since different nuclei have different spin values and different masses, each nuclei has a distinct gyromagnetic ratio value. Ultimately, the gyromagnetic ratio is important in determining how much signal is detected from the precession of a given nuclei. In this study we exclusively studied proton nucleus, which has a gyromagnetic ratio ($\gamma/2\pi$) of 42.577 MHz/T.

1.1.3 Interaction with Radio-Frequency field

When a magnetic field B_1 is applied orthogonal to the static magnetic field and at the resonant frequency, it will exert a torque on the magnetization vector resulting in the vector $\overrightarrow{M}$ initially rotating away from the equilibrium position z and precessing around the z-axis towards the transverse plane (x-y plane). If we define a rotating frame of reference, which rotates about the z-axis at the Larmor frequency, x and y axes are now defined as x' and y' and the magnetization vector rotates as shown in Fig. 1.3. Similar to the Larmor relationship, the frequency of rotation of the

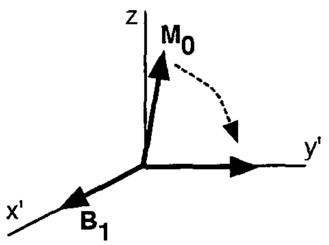

Fig. 1.3: B_1 magnetic field applied to the magnetization vector

magnetization vector away for the z-axis can be expressed as

$$\omega_1 = \gamma B_1. \tag{1.7}$$

Following this excitation, the magnetization vector behavior will be related to two relaxation processes. The transverse component of the magnetization decays away with a relaxation time constant of T_2, and the longitudinal component approaches its initial equilibrium state with a relaxation time constant of T_1 . The parameters ρ_0, T_1 and T_2 are responsible for multiple imaging contrast possibilities, which makes MRI an invaluable diagnostic tool compared to other imaging modalities.

Now, the basic NMR experiment can be described by explaining the interaction between a simple coil and the sample to be imaged. If an alternating current is passed through a simple coil, and provided that the angular frequency of the current is very close to the nuclei's corresponding Larmor frequency, the magnetization vector will be excited and tipped towards the transverse plane, as previously described. For a given tip angle θ, the RF must be applied along a direction perpendicular to the static magnetic field (see Fig. 1.4). B_1, the angle θ and the RF period time (τ) are related by the following equation

$$\theta = \gamma B_1 \tau. \tag{1.8}$$

Once the magnetization vector is in the xy-plane, the voltage applied to the coil

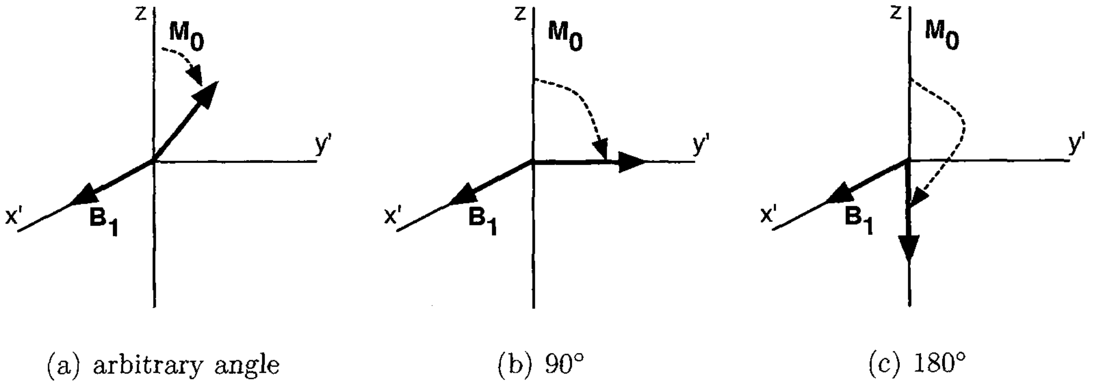

(a) arbitrary angle (b) 90° (c) 180°

Fig. 1.4: Examples of tip angles in the rotating frame. (a) arbitrary pulse, (b) 90° pulse, (c)180° pulse. The magnetization starts from the equilibrium direction and is represented in the rotating frame of reference

can be stopped and the transmit operation can be considered complete. Following the excitation process, from Faradays law of induction, the precessing magnetization vector induces a measurable electromotive force (EMF) in the RF coil (now in receiving mode). In certain designs, the coil generating the RF excitation field will switch modes and receive the signal as well. The result of this process generates a time signal commonly called free induction decay (FID) and is characterized by an exponential decay with time constant of T_2^* , oscillating at the Larmor frequency (see Fig. 1.5).

$$S = M_0 \sin\alpha \cdot e^{-\frac{t}{T_2^*}}. \tag{1.9}$$

1.1.4 Encoding Principles and Fourier Transform

In the context of MR imaging, the objective is to map the spatial distribution of the amplitudes of all the spins obtained through the FID and create the corresponding image. If each spin were to experience a distinct magnetic field, then spatial discrimination of the region would be possible, based on the different frequencies of all the spins. To achieve such property a gradient in the magnetic field is used. The magnetic field gradient is a variation in magnetic field strength based on position and can be applied in the x, y, or z directions. We now examine how this process works.

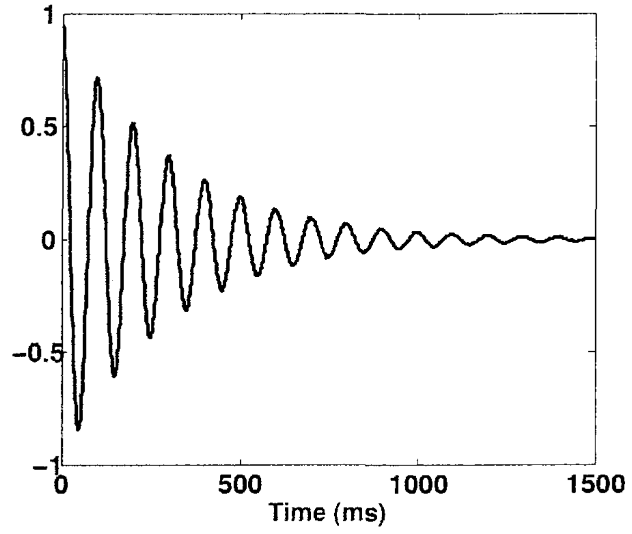

Fig. 1.5: FID, free induction decay

First, let's define a gradient along the z-axis as the slice select gradient. For our example this implies that the z-axis is perpendicular to the plane of our desired image. If we then consider the center of the scanner (isocenter) to have a magnetic field of B_0 and a frequency of f_0 at z_0 , when a linear magnetic field gradient is applied along the z direction, the frequency and the position will be related by the following equations

$$f(z) = \gamma(B_0 + zG_z) = f_0 + \gamma z G_z \qquad (1.10)$$

$$z = \frac{f - f_0}{\gamma G_z} \qquad (1.11)$$

where z is the position along the z-axis and G_z the gradient field (normally measured in millitesla/meter). This procedure will excite a slice at location z, as long as the RF pulse is tuned to the frequency $f(z)$. In a 2D imaging scenario, only the spins present in the z locations that have the same resonant frequency as the angular frequency bandwidth of B_1 will be excited, leaving unaltered all the spins outside of this area. This slice selective excitation is determined by the bandwidth $\gamma\Delta z G_z$, centered about

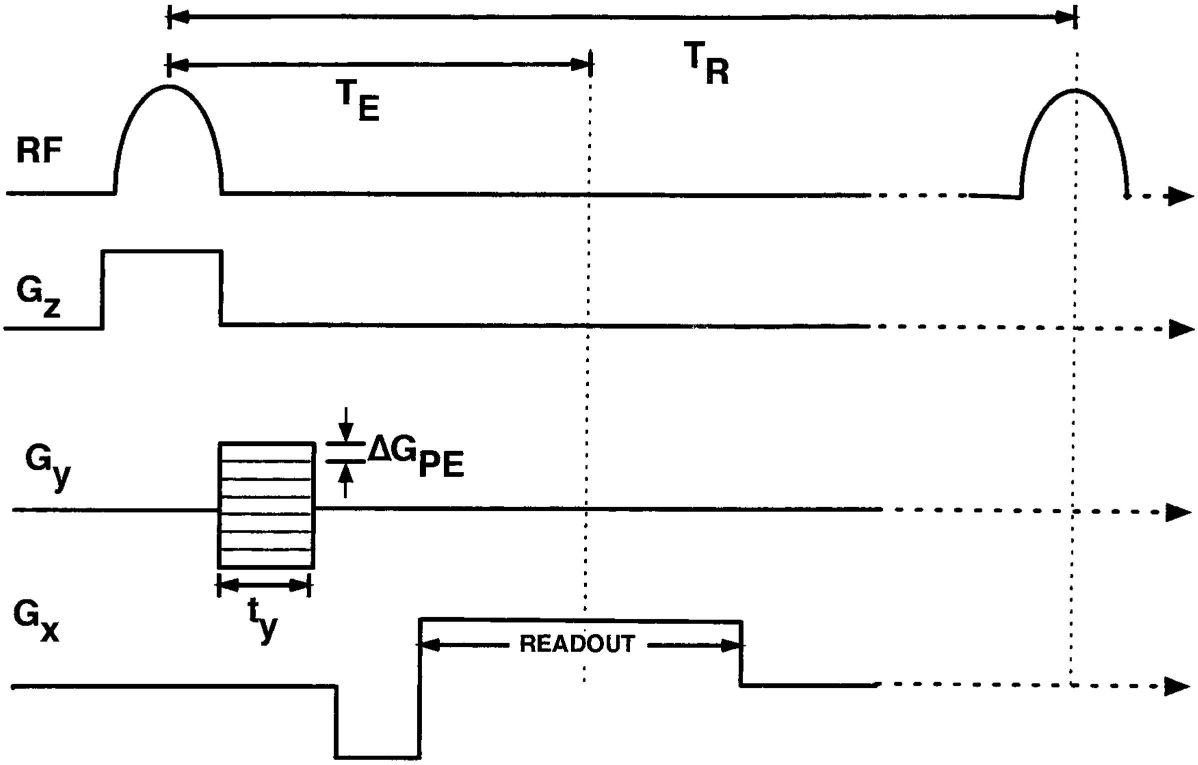

Fig. 1.6: A generic 2D echo pulse sequence

f_0 for an excitation of a slice in the plane z = 0.

Second, after the slice select gradient is turned off, the phase encoding gradient is applied. Usually, the y-gradient G_y, is used to exert a spatial-dependent phase angle to the excited spins. Therefore, the magnetization accumulates a y-dependent phase, for the time that the y-gradient is applied (τ_{PE}), that can be expressed as

$$\phi(y,t) = -\gamma y \int_0^{\tau_{PE}} dt G(t). \tag{1.12}$$

The G_y gradient will be increased or decreased every cycle during an image acquisition, by steps of ΔG_{PE} (or ΔG_y), to obtain the information about the spin density along the y-direction (see Fig. 1.6).

The third gradient magnetic field is applied along the x-direction, also called the read gradient. During the application of G_x the signal is actually sampled and

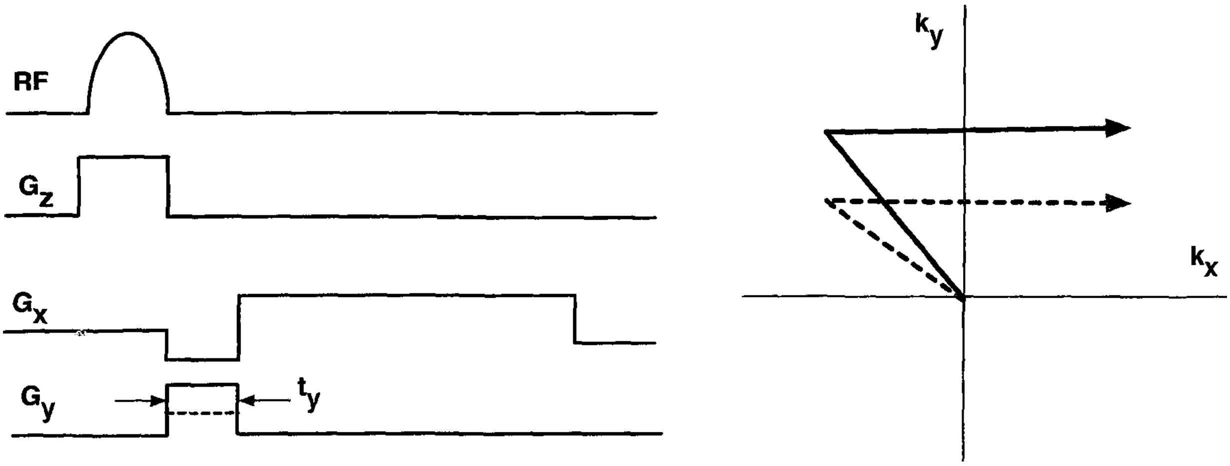

Fig. 1.7: 2D Fourier Transform sequence, with the timing diagram (left) and the corresponding k-space trajectory (right).

acquired. The resonance frequency is proportional to the position of the spin. How this information is "translated" into an image is explained through the introduction of the concept of *k-space.*

If we now introduce a new parameter (k) as a spatial-frequency variable, with units of inverse distance (m^{-1}), each sampled point can be referred as a point in what is commonly known as the frequency space or *k-space.* In fact, the pulse sequence described in Fig. 1.6, maps a specific trajectory in the k-space domain. The trajectory (see Fig. 1.7) can be expressed by the time integrals of the applied gradients G_x and G_y as follows

$$k_x = \frac{\gamma}{2\pi}\int_0^t G_x(\tau)d\tau \tag{1.13}$$

$$k_y = \frac{\gamma}{2\pi}\int_0^{T_y} \Delta G_y(\tau)d\tau. \tag{1.14}$$

When sufficient k-space lines are acquired, a two dimensional image can obtained by the simple inverse 2D Fourier transform of the acquired signal. This rectilinear method of sampling is known as a Cartesian k-space method. The equation that

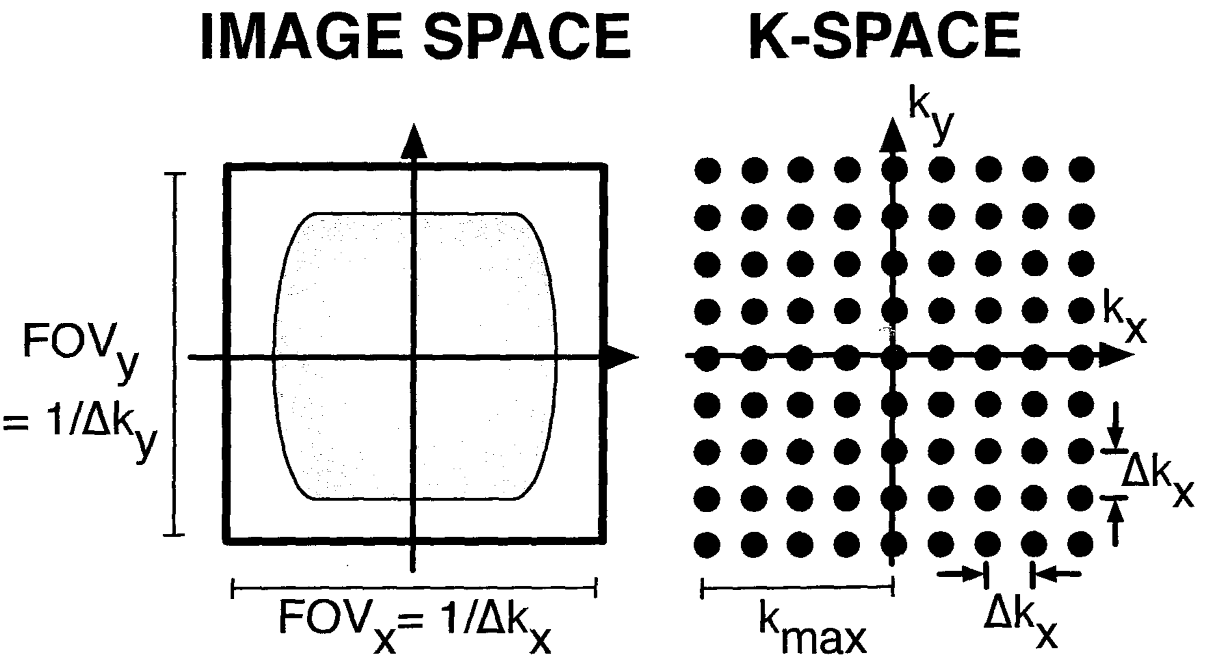

Fig. 1.8: Illustration of sampled k-space (right) and its corresponding representation in image space

describe the Fourier transform relationship between the signal acquired and the final image is as follows:

$$m(x, y) = \Im^{-1}\{s(k_x, k_y)\} \tag{1.15}$$

where $m(x, y)$ is the image space signal and $s(k_x, k_y)$ is the frequency space. The magnitude of the gradient relates to k_x and k_y with Eqn. 1.13 and Eqn. 1.14. The resolution of a final MR image is determined by the k_{max}, the highest spatial frequency sample in k-space, while the field of view (FOV) is determined by the sampling interval Δk, shown in Fig. 1.8.

$$FOV_x = \frac{1}{\Delta_{k_x}} = \frac{1}{\frac{\gamma}{2\pi} Gx \Delta t} \tag{1.16}$$

$$FOV_y = \frac{1}{\Delta_{k_y}} = \frac{1}{\frac{\gamma}{2\pi} \Delta Gy \tau_y} \tag{1.17}$$

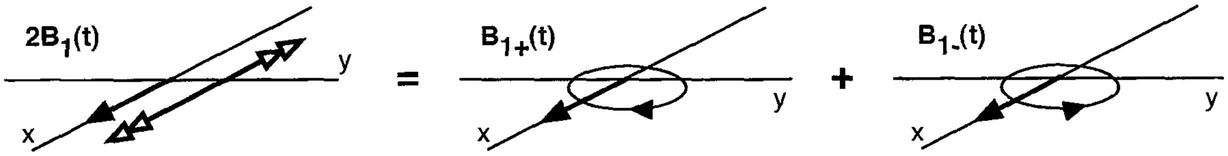

Fig. 1.9: Linearly polarized vector here is shown applied in the transverse plane and decomposed in the counter-rotating circularly polarized fields.

1.2 Polarization and Radio-Frequency Wavelength Effects

Herein we introduce the concept of polarization which provides more details regarding the RF magnetic field B_1. The vector describing the amplitude-modulated RF pulse $\vec{B}_1(t)$, is defined as a linearly polarized magnetic field, generated by a single RF coil and can be written as

$$\vec{B}_1(t) = 2B_1(t) cos\omega t \; \vec{x} \tag{1.18}$$

where ω is the carrier frequency of the excitation (please note that in the previous section the time dependence of the amplitude of $\vec{B}_1$ had been ignored for simplicity). The linearly polarized field can be decomposed into two circularly polarized fields (see Fig. 1.9), which are described by the following equation:

$$\vec{B}_1(t) = B_1(t)(cos\omega t \; \vec{x} - sin\omega t \; \vec{y}) + B_1(t)(cos\omega t \; \vec{x} + sin\omega t \; \vec{y}) \, . \tag{1.19}$$

The first component of the vector rotates clockwise and the second component rotates counterclockwise. What's important here is that only half of the linearly polarized magnetic field contributes towards tipping the spins, in fact, only $B_1(t)(cos\omega t \; \vec{x} - sin\omega t \; \vec{y})$, has a relevant effect to the magnetization because it rotates in the same direction as the precessing spins. The effects on the final image of the circularly polarized vectors rotating in the same direction and the opposite direction as the precessing magnetization vector, is shown in Fig. 1.10. Ultimately, the benefits related to RF power deposition and SNR, prompts most MR imaging system to utilize quadrature coils. These type of coils are constructed with a symmetrical design that produces two modes, which are spatially and electrically orthogonal. Quadrature excitation of the two modes with currents of equal magnitude but with phases differing by 90°, produces a circularly polarized RF field. For a given flip angle, circularly polarized fields require half of the power required for linearly polarized fields and similarly quadrature reception also improves SNR by $\sqrt{2}$.

In ultra-high field, RF interaction with the sample becomes a challenge as the RF wavelength approaches the size of the target object [4–6]. In this condition images acquired with a volume coil display a very strong B_1 magnitude and signal intensity in the center compared to the periphery. This phenomenon is the result of interference between reflected and refracted RF traveling waves though the sample. This phenomenon has been called "standing wave effect" or "dielectric resonance effect". However, the high intensity is not really a consequence of dielectric resonance, rather is the result of phase combination (or partial combination) of the superimposed RF traveling waves [7, 8]. (The implications of circularly polarized vectors, quadrature coils and RF wavelength phenomenon will be discussed in later chapters in greater detail).

1.3 Parallel Imaging

Historically, MRI has evolved by improving SNR and reducing image acquisition times. Scan times have been successfully reduced primarily by improving system hardware (e.g., fast switching gradients) and developing fast imaging sequences (e.g., EPI, Spiral). Unfortunately, extremely fast switching gradients can induce peripheral nerve stimulation and as a result some system limitations need to be put in place to reduce operation speed. Today most clinical scanners operate just below these

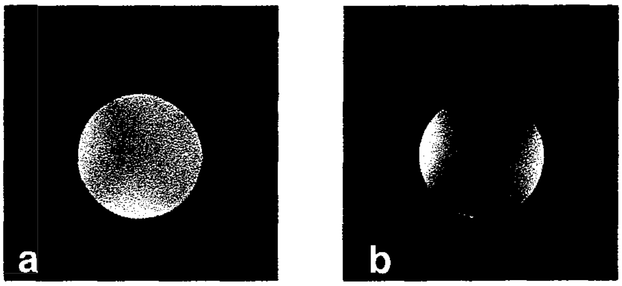

Fig. 1.10: In this figure a four-element transceive array coil is driven in quadrature mode (a), where the elements during excitation and reception are driven with phase differing by 90°. This creates a circularly polarized field rotating in the same direction as the precessing spins. When the four elements are driven in anti-quadrature mode (b), the circularly polarized vector induced rotates in the opposite direction and voids are created because this vector is inefficient in tipping the main magnetization vector. Note that in (b), the circularly polarized components created are not perfectly circular, but rather elliptical, which explains the imperfect signal voids.

limits, which suggests that additional acquisition time reduction cannot be achieved by gradient improvement alone [9–11]. Fortunately, parallel imaging can overcome hardware and pulse sequence limitations and reduce overall scanning time by reducing the number of k-space data acquired.

As stated in Sec. 1.1.4, the total imaging time for rectilinear scanning is determined by the gradient magnitude, and the time to reach the limit of the k-space extent (for simplicity we assume the extent is fixed to keep the resolution the same). Therefore, if the objective is to reduce scan time, Δk needs to increase as much as possible in order to reduce the overall number of steps required to cover the k-space extent. Recalling the relation in Eqn. 1.16 and Eqn. 1.17, increasing Δk results in a decreased FOV in image space and when the FOV does not wholly contain the sample being imaged, the regions outside the FOV are wrapped and produce an aliased image as shown in Fig. 1.11. The reduction factor R, also known as the acceleration rate indicates the factor by which the number of k-space steps are reduced.

The object of parallel imaging, in its simplest form, is to "unwrap" the folded images, and reconstruct full images with the same field of view and spatial resolu-

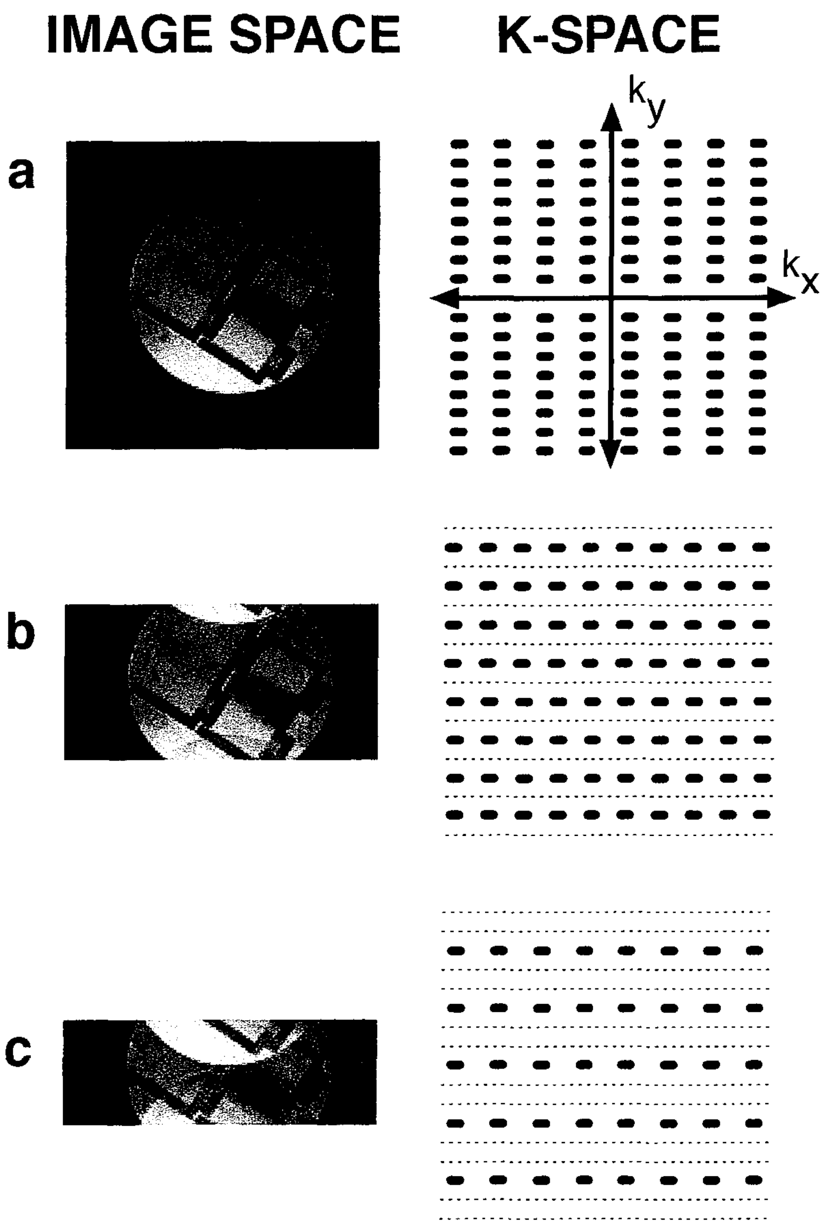

Fig. 1.11: Magnitude images for three different sampling rates are shown on the left column. The corresponding k-space sampling rates on the right (heavy dotted line represents data collected, light dotted line represents data not acquired). A fully sampled image is shown in a. As k-space is under-sampled in the k_y direction (for both b and c), the FOV drastically decreases and aliasing can be seen along the y-axis in image space. In parallel imaging, images b and c correspond to R=2 and R=3 reduction rates respectively.

images, and reconstruct full images with the same field of view and spatial resolution as the equivalent, conventionally acquired, MR images. To implement parallel imaging, the system requires independent multiple receive coils with distinct sensitivities across the sample being imaged. That information is used to distinguish and then separate the overlapped pixels. Although, novel spatial encoding concepts had been discussed, it wasn't until Sodickson with Simultaneous Acquisition of Spatial Harmonics (SMASH) in 1997 [12] and Pruessman in 1999 with Sensitivity Encoding (SENSE) [13], that successful in vivo results were shown and that the MR community finally embraced the practicality and feasibility of these fast-imaging methods. The details and the mathematics that describe both SENSE and "generalized auto calibrating partially parallel acquisition" (GRAPPA [14], an extension of SMASH) are well explained in the respective topical papers therefore an overview of these methods is given in this section to explain the relationship between these reconstruction techniques and RF coil design.

In SENSE, the image processing is performed in image space. In this reconstruction method the key information comes from the receiver coil itself. With a receiver coil placed near the object, the contribution of a signal source to the induced voltage varies with its relative position. In other words, the knowledge of the so called sensitivity maps implies spatial information about the origin of detected MR signals. Thus, in the simple example of Cartesian reconstruction, the first step consists of calculating the sensitivity maps and acquiring accelerated data (which results in an aliased image) for each receiver coil available in the system. The second step involves unfolding the aliased image on a pixel by pixel basis, via matrix inversion, to recreate the full FOV image. The key of the unfolding process is that each superimposed pixel signal is the result of the contribution of several pixels that in each coil image have different weight, according to the coil sensitivities. The sensitivity information is used to calculate the unfolding matrix U, which can be expressed as:

$$U = (C^H Y^{-1} C)^{-1} C^H Y^{-1}, \tag{1.20}$$

where C is the coil sensitivity matrix, and Y is the noise matrix. The matrix Y can be estimated through the analysis of data acquired in the absence of MR signal. If η_{ij} represents the noise sample acquired by coil i, Y_{ij} entry of the matrix is given by

$$Y_{ij} = \overline{\eta_i \eta_j^*} \tag{1.21}$$

with the bar indicating time averaging. Although this matrix can be replaced by the identity matrix (which represents the ideal case with zero noise), it's important to take into account possible differences in noise levels and the noise correlation between different coil channels by including the actual noise matrix. And finally the pixel-wise reconstruction is obtained by the following

$$\rho' = U \cdot \vec{S} \tag{1.22}$$

where ρ' is the reconstructed spin density and $\vec{S}$ is a vector representing the complex coil images values at the chosen pixels in the aliased image with length equal to the number of coils. Thus, unfolding is always possible as long as the number of pixels to be separated does not exceed the number of available coils. In the final reconstructed image each pixel is multiplied by a different weighting factor, according to the coil sensitivity maps, making the final image correspond to the ideal reconstruction proposed by Roemer in [15]. The SNR in all MRI images is governed by the relation

$$\mathrm{SNR} \propto \Delta x \Delta y \Delta z \sqrt{N_{average} N_y T_{read}}. \tag{1.23}$$

Therefore, reducing the number of phase encodes, reduces the total acquisition time ($= N_{average} N_y T_{read}$) and when resolution is kept unchanged, SNR is decreased by

$$\mathrm{SNR}_{\mathrm{red}} = \frac{\mathrm{SNR}_{\mathrm{full}}}{g\sqrt{R}} \tag{1.24}$$

where SNR_{full} represents an acquisition with $R = 1$ (no reduction) and SNR_{red} represents an acquisition with $R = 2, 3, 4, ...$ The g-factor is always at least equal to 1: so in a g-factor map, values equal to 1 represent the best case scenario, whereas higher values indicate regions of higher noise propagation. It depends on the coil geometry, and generally indicates the ability to perform the matrix inversion and separate aliased pixels. In practice it allows *a priori* SNR estimates and provides an important criterion for the design of dedicated coil arrays [13].

As previously mentioned GRAPPA is an extension of SMASH and they are both defined as k-space based methods, since the data manipulation occurs in the k-space domain. In SMASH, the coil sensitivity maps are used to repopulate the missing k-space lines that would normally be acquired using phase encode gradients. To understand how this is process occurs it's important to note that a phase encode gradient imparts a sinusoidal modulation across the whole object and the higher the gradient strength-time product during the gradient application, the higher the number of cycles of the sinuoisdal wave. Coil arrays can provide spatial information about a sample by emulating the spatial modulations produced by the gradients that have been skipped from the acquisition. This is the basic idea behind SMASH. The coil sensitivities are fitted to approximate the spatial harmonics (that is to extrapolate the ideal phase encode shifting functions), to populate the missing k-space lines. Thus, the sensitivity profiles are multiplied by the linear weight of each coil to produce the mth spatial harmonic, as shown in

$$\sum_{j}^{N_c} w_j^m C_j(x, y) = e^{-im\Delta k_y y} \tag{1.25}$$

where j is the index from 1 to N_c number of coils, w_j^m is the linear weight, m is the order of the spatial harmonic generated, C_j represents the coil sensitivity for the jth where j is the index from 1 to N_c number of coils, w_j^m is the linear weight, m is the order of the spatial harmonic generated, C_j represents the coil sensitivity for the jth coil and $\Delta k_y = 2\pi/FOV$. The effect of applying the linear coefficients, w_j^m, is to move the acquired data in k-space by a distance $m\Delta k$. The measured signal $S_j(k_x, k_y)$ is then used to calculate the spin density $\rho_{(x,y)}$ (and reconstruct the image) via inverse Fourier Transform, as show in

$$S_j(k_x, k_y) \sum_j w_j^m \approx \int \int \rho_{(x,y)} e^{-ik_x k_y xy} e^{-im\Delta k_y y} dxdy. \tag{1.26}$$

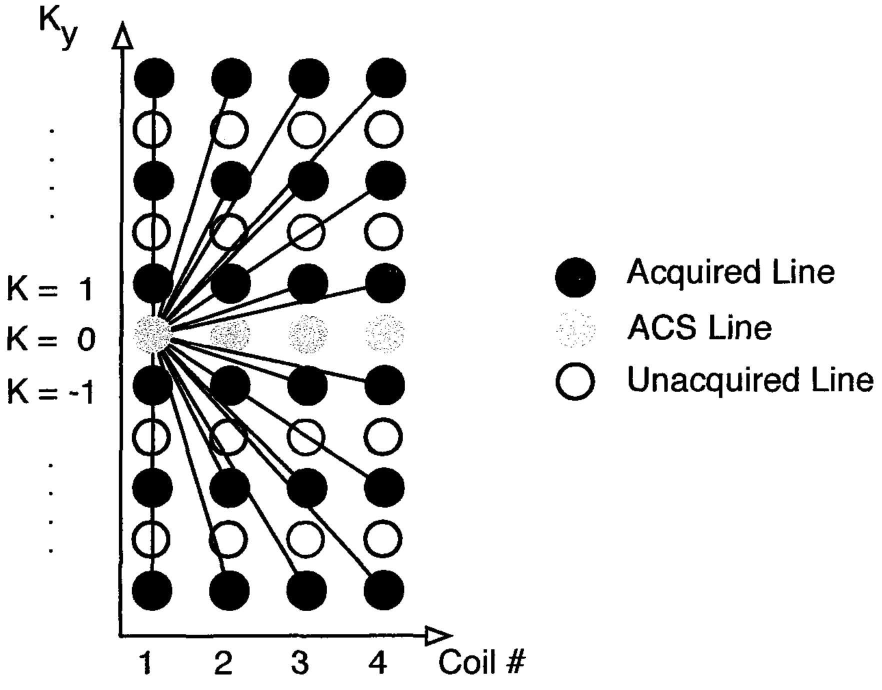

Fig. 1.12: The basic GRAPPA algorithm is shown schematically. In GRAPPA, more than one line acquired in each of the coils in the array are fit to an ACS line acquired in a single coil of the array. This fit gives the weights which can then be used to generate the missing lines from that coil. In this case, four acquired lines are used to fit one ACS line in coil no. 1. Acquiring multiple ACS lines allows for multiple fits which mitigates noise effects and imperfections in the sensitivity maps. This example shows an acceleration factor of two

The accuracy of the reconstructed line $S_j(k_x, k_y + m\Delta k)$ depends on the acccruacy of the linear fit in Eqn. 1.25. From a coil design perspective, ideally one needs to design a coil array that has a linear combination that best approximates the spatial harmonics.

A feature of GRAPPA reconstructions is that separate images are reconstructed for each coil. These can be combined finally by any means desired (typically SOS). In order to determine the reconstruction weights the following expression is employed:

$$S_j(k_x, k_y + m\Delta k) = \sum_l \sum_b w(j, b, l, m) S_l(k_x, k_y + br\Delta k). \tag{1.27}$$

where r is the acceleration factor, b is an index that counts through the multiple lines used in the reconstruction and l is an index that counts through the number of coils. The major advantage of GRAPPA over SMASH is that coil weighting information w_j^m is not obtained by direct calculation of the sensitivity maps, but rather it is estimated by acquiring a few extra lines of k-space, called auto-calibration signal (ACS) lines. The lines of the reduced data set are fit to the ACS lines to determine the set of linear weights w_j^m. Generally, $R - 1$ extra ACS lines are acquired around the center of k-space, which means that for an acceleration factor of 2, only a single extra k-space line is required, but in practice many more are used to improve the reconstruction. We are able to extrapolate spatial sensitivity information from only a few ACS lines because the spatial frequency variation of the coil sensitivity is very low. A schematic description of a GRAPPA acquisition is shown in Fig. 1.12.

In contrast to a SMASH complex sum image reconstruction, the GRAPPA algorithm results in uncombined single coil images, which can be combined using a magnitude reconstruction procedure (eg, sum of squares). This provides a significantly improved SNR performance, especially at low reduction factors. Furthermore, signal losses due to phase cancellations are essentially eliminated using a magnitude reconstruction procedure.

Finally, if accurate coil sensitivity maps are available, it is preferable to use SENSE where the sensitivity information is directly calculated, as opposed to GRAPPA, which is an approximate solutions resulting from a fit to spatial harmonics. However, there are cases when obtaining precise coil sensitivity data may be difficult and in these cases the fitting procedure of GRAPPA will give produce less errors in the final image.

1.4 Imaging Hardware

The previous sections have described the magnetization vector and the electromagnetic forces operating on it; however, the hardware responsible for producing such forces has only been mentioned briefly. The following sections will describe the essential components that constitute a MR system. Essentially, if one was to simplify the hardware involved in producing the magnetic forces down to its basic structure, the result would be reduced to the three essential components: the main magnet, the gradient coils, and the RF coil. The main magnet produces a B_0 field for the imaging process and defines the z-direction. The gradient coils produce the gradient in B_0 in the x, y, and z directions. And finally, the RF coil produces the B_1 magnetic field necessary to rotate the spins during the excitation phase. Additionally, the RF coil also detects the signal from the spins within the body.

1.4.1 Main Magnet

The objective of the main magnet is to align the population of spins parallel to the magnetic field producing a positive net magnetization. There are several types of magnets, however most magnets used for clinical and research application are of the superconductive type. This magnet is made of superconducting wire with a resistance approximately equal to zero when it is immersed in liquid helium and cooled down to 0 K or -273.15 °C (absolute zero). Once the current flows in the coil it will continue to flow if the coil is kept at liquid helium temperatures, and even after the current source is disconnected, it yields a very stable field.

1.4.2 The Gradient Coils

As previously stated, linear magnetic field gradient coils are used to spatially encode the positions of the nuclear spins in the MRI system by varying the value of the local magnetic field, causing precessional frequencies or phases to vary as a function of their positions. A gradient coil set is made up of three coils that produce the x, y and z-gradients. Gradient coils are rapidly turned on and off and current is induced to create positive and negative field strengths. Essential requirements for the field produced are linearity over the imaging volume, low inductance, high current to gradient ratio and minimal resistance

1.4.3 The RF Coils

In MR there are a great variety of coil designs, mostly dictated by the application and the sample size. However, at its core it is possible to divide coils into three main groups: transmit coils which are required to produce a uniform B_1 field over the region of interest, receive coils which are required to ensure high sensitivity over the volume being imaged, and transmit/receive (transceive coils). Although separate coils for transmit and receive operation have been widely used, our desired requirements and modes of operation demand the use of transceive coils. The next chapter will describe in greater detail the process and challenges in building an RF coil.

Chapter 2

RF Coils Design Principles

2.1 Introduction

In this chapter the fundamentals of RF coil design will be presented. The terms *coil, resonator* and *probe* may be used interchangeably from now on to describe the main RF device. We will introduce the concepts of signal, noise, tuning, matching and balancing relative to the coil and its construction. These basic design principles apply to all coil designs regardless of complexity, and they all aim to increase the efficiency of the resonator. The description of RF coil design will begin with a simple conductive loop of wire to demonstrate the transmission and reception process.

In the case of a conductive loop of wire, the precession of the magnetization vector is able to generate an electromotive force (EMF), which induces current in the receiving loop when it is closed by a circuit. By reciprocity, when a current is passing through that loop wire for a limited period of time, it can excite a sample and alter the magnetization vector within that sample. Fundamentally, the loop of wire is an example of the most simple coil design, and it can be modeled as an RLC circuit, which is an electrical circuit consisting of a resistor (R), an inductor (L), and a capacitor (C) that follows electrical resonant circuit properties. Therefore in our example, the EMF signal induced in the coil loop will be multiplied by Q (the quality coefficient of the resonator circuit) and if the resonator is matched to the system impedance (typically 50Ω) and tuned to the system frequency ($f_0 = \gamma B_0$), it will carry a combination of useful signal and unwanted noise (both multiplied by Q). Thus, an RF resonator must be tuned to filter out unwanted frequencies, must be impedance matched to deliver and/or receive the signal with the highest efficiency, and designed to minimize all possible sources of noise.

2.2 Signal and Noise Sources

Signal induced in a coil depends on a variety of factors. The signal evaluation is described by Hoult *et al.* [16] using the reciprocity principle. As mentioned in Sec. 1.1.2, in proton imaging the total magnetization (M_0) in the sample volume (V_s) is given by the following relation

$$M_s = M_0 V_s \tag{2.1}$$

where

$$M_0 = \rho_0 \frac{\gamma^2 \hbar^2}{4kT} B_0. \tag{2.2}$$

The EMF signal is induced by the time changing magnetic field, and can be written as the following,

$$\xi = \omega_0 (B_1)_{xy} M_s \cos(\omega_0 t) \tag{2.3}$$

where $(B_1)_{xy}$ is the magnetic component perpendicular to the main magnetic field and $\cos(\omega_0 t)$ is the time dependent amplitude modulating factor. Since $\omega_0 = \gamma B_0$, it follows that the EMF signal induced in the coil is proportional to the square of the main field strength.

Having considered the signal, we can now introduce the noise component. Based on thermodynamics principles, the noise in the coil is given by

$$\sigma = \sqrt{4kT_{coil}\Delta f R_{\text{eff}}} \tag{2.4}$$

where k is the Boltzmann's constant, T_{coil} is the temperature of the coil, Δf is the bandwidth of the system and R_{eff} is the effective resistance in the system. The effective resistance is generally the summation of various components as such:

$$R_{\text{eff}} = R_{\text{coil}} + R_{\text{sample}} + R_{\text{electronics}}, \tag{2.5}$$

although in small animal imaging coil noise is the dominant noise [17], we will also describe other possible noise sources.

Power dissipation results from any current flowing through the resistive conductive material. The coil resistance depends on conductivity (or resistive) properties of the material; however, the biggest contributing factor to resistance increase is actually frequency-related. The resistance of the conductor increases with the frequency, due to the skin depth effect and proximity effect. The skin depth effect occurs as a result of the presence of eddy currents, which contribute to electric currents flowing near the surface of the conductor, reducing the overall cross-sectional area current density and increasing the resistance. Similarly, the proximity effect occurs when current flowing through a conductor creates a magnetic field that influences or even cancels the current distribution of an adjacent conductor. These effects are significant when high frequency AC current is applied, increasing the overall losses. The frequency-dependent resistance of a rectangular conductor is defined as:

$$R \approx \frac{\rho L \sqrt{\pi f \mu \sigma}}{2W + 2H} \tag{2.6}$$

where W, H and L are respectively the width, the height and the length of the conductor, $(\pi f \mu \sigma)$ is the skin depth factor and finally ρ is the conductor resistivity (and not the density of spins per unit volume ρ_0). To minimize these losses great care needs to be taken during coil construction and component selection as explained in

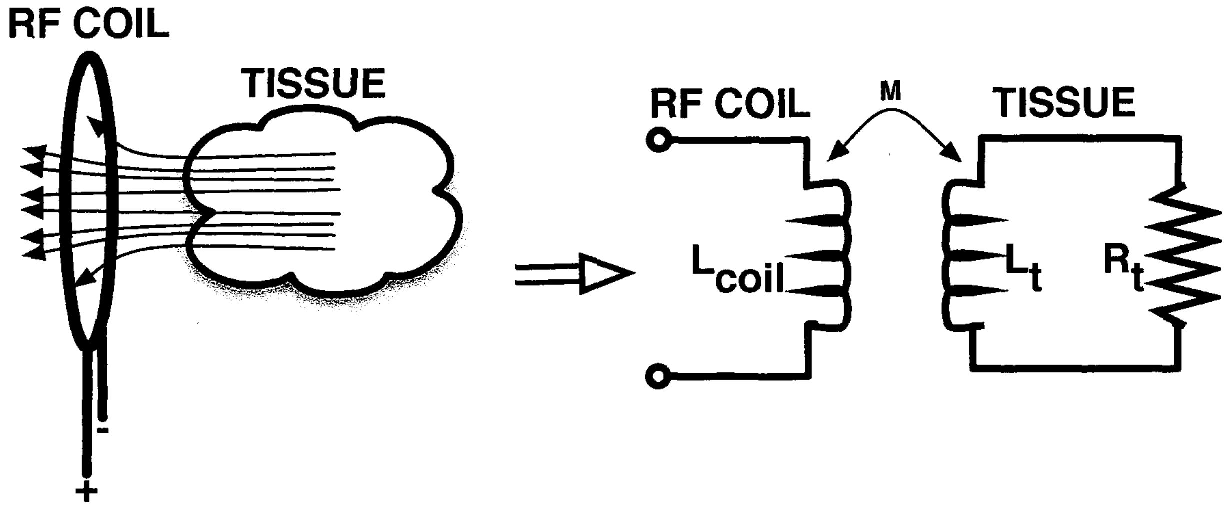

Fig. 2.1: Modeling of coil-to-tissue interaction. Currents in the body couple inductively with the coil through their respective inductance L_t and L_{coil} when placed in close proximity. The mutual inductance is represented as M.

the remainder of this chapter.

Tissue loss (or sample noise) can result from randomly occurring current loops within the sample that inductively couple to the RF coil and also from the increased resistance of the surface coil due to electric field power dissipation in the patient. The coupling effect can be modeled as a transformer circuit as shown in Fig. 2.1. Sample noise, usually dominant in coils in high field human systems, can be minimized by balancing the coil with respect to the sample or (the electrical ground) (see balancing in Sec. 2.4).

Electronics loss is a general term to identify losses that relate to the equipment used or specific hardware design shortcomings. Radiation losses for example, occur when the coil acts as a "far-field" conventional antenna, that is when the coil size is of the same order as the operating wavelength. From the principles of antenna theory, we know that in a small loop antenna, the amount of radiated energy is proportional to the power of the operational frequency ω_0 [18] and therefore it increases with main magnetic field. Also, electrical losses usually arise because of potential differences

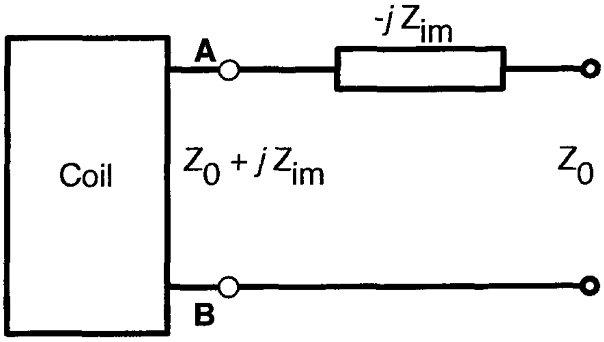

Fig. 2.2: Here is shown the general impedance matching strategy. The first step is to adjust the coil components so that the impedance at port-AB is equal to Z_0 (at ω_0), the second step is to compensate the reactive component with by adding an adjustable conjugage impedance, -jZ_{im}.

between ground and some circuit parts, creating high frequency electrical field through the sample or other components. Radiation losses as well as electrical losses can be minimized through careful balancing of the circuit which will be explained in more detail in Sec. 2.4 below.

Finally, we can derive an equation for coil SNR. The generic definition of SNR is

$$\mathrm{SNR}_{(dB)} = 10\ log_{10}\left(\frac{V_0^2}{V_n^2}\right) \tag{2.7}$$

the V_0^2 and V_n^2 are the voltages of the signal and noise respectively, with SNR expressed in decibels. Therefore from Eqns. 2.3 and 2.4 it follows that SNR for a loop coil is

$$\mathrm{SNR}_{(dB)} = 10\ log_{10}\left(\frac{\xi^2}{4kT_{coil}\Delta f R_{coil}}\right). \tag{2.8}$$

However, it is important to note that the above equation, which is a practical definition of SNR, is not sufficient in evaluating phased array coils or preamp-decoupled coils (the equation does not take into account neighbouring coil coupling noise), so it should only be used as a reference to improve the coil performance.

2.3 Tuning and Matching

As previously mentioned, the simple loop coil can be modeled as an RLC circuit. Because the characteristic impedance of an electrical circuit is $Z = a + jb$, formed by a resistive component a and a reactive component b, for a series RLC circuit the impedance Z_{AB} of the circuit is

$$Z_{AB} = r + JL\omega + \frac{1}{jC\omega} = r + j\left(L\omega - \frac{1}{C\omega}\right) \tag{2.9}$$

where r is the resistive impedance. The objective of the design is to transform Z_{AB} in a purely resistive impedance (with zero reactive impedance), which according to Eqn. 2.9 occurs when

$$L\omega = \frac{1}{C\omega}. \tag{2.10}$$

This condition only occurs for one frequency ω_0 (when the capacitor impedance compensates precisely the inductor impedance), which also defines the well known *resonant condition*, where

$$\omega_0 = \frac{1}{\sqrt{LC}} \tag{2.11}$$

or

$$f_0 = \frac{1}{2\pi\sqrt{LC}}. \tag{2.12}$$

When the circuit is in the resonant condition, the capacitor and the inductor begin to exchange energy at every cycle, which also dissipates slowly in the resistive component r. For the ideal RLC circuit at the resonant condition, the real part of Z_{AB} remains constant to the value of r for all frequencies. However, at the tuned frequency, the RLC circuit produces a Z_{AB} value that is lower or higher than the required Z_0 (50 Ω typical for most systems, to deliver and/or receive signal with the highest

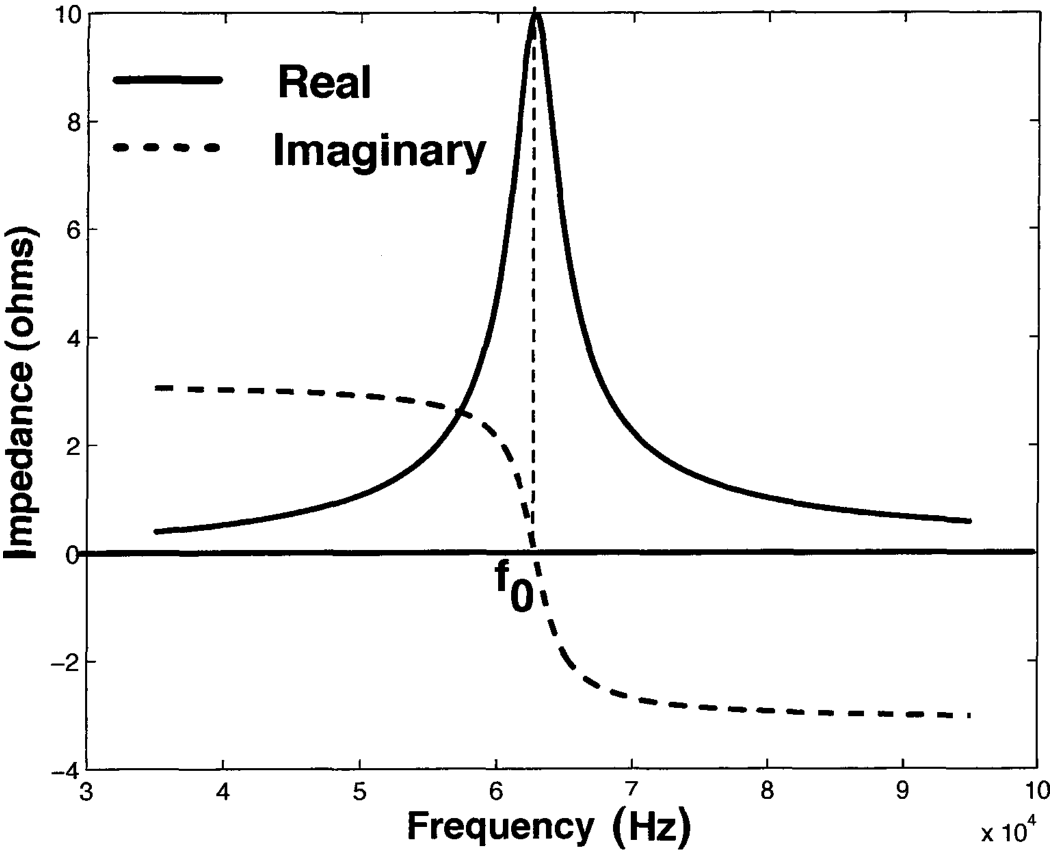

Fig. 2.3: Impedance frequency dependence of an RLC circuit. The graph shows both the real and imaginary components. Both are necessary to establish matching at 50Ω and tuning at 400 MHz.

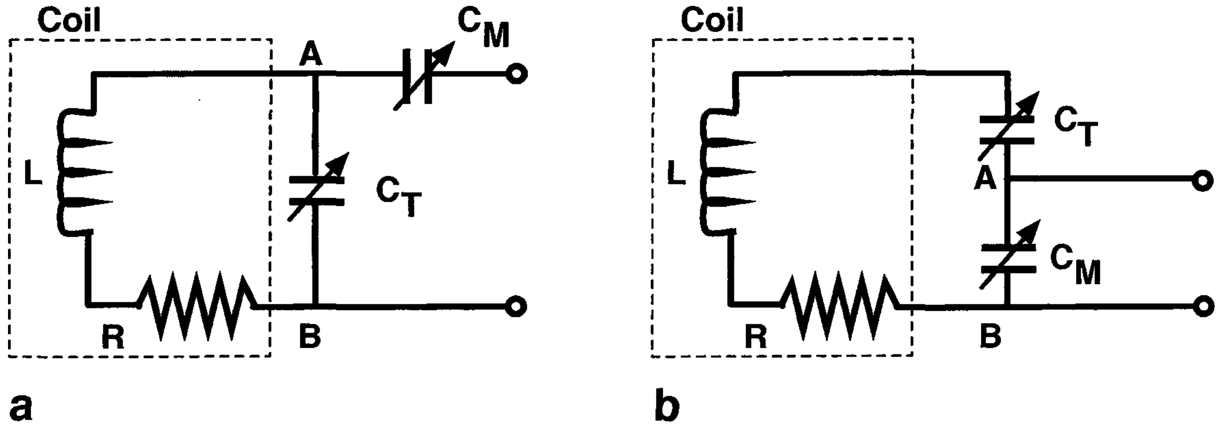

Fig. 2.4: Capacitive matching networks: (a) series capacitive matching network, (b) parallel capacitive matching network. Capacitive decoupling is necessary in the case where the reactive component is positive (inductive) as it can only be compensated by a (high quality variable) capacitor.

efficiency). Thus, to accomplish the matching a few steps need to be followed. First, the capacitors and/or inductors in the circuit must be adjusted such that the resistive impedance at the AB port is equal to Z_0. Second, the reactive component must be compensated at this frequency, by connecting an appropriate adjustable conjugate impedance $-j[Z_{im}(\omega_0)]$, (Fig. 2.2).

There are two general ways to perform impedance matching in a resonant circuit using an oscilloscope. Referring to Fig. 2.3, in the first case the frequency of the tuned circuit is chosen to be slightly higher than the wanted f_0; therefore, the imaginary component of Z_{AB} is positive and the circuit can be compensated by a capacitor in series. In the second case, the frequency of the tuned circuit is set lower than f_0, so that the imaginary component becomes negative and can be compensated with an inductor. The former method is generally preferred to the latter method, because of the lossy nature of inductors and the difficulty of building high quality and non-magnetic variable inductors.

Fig. 2.4(a) and Fig. 2.4(b) show capacitive matching in a series and parallel configuration respectively. This is the case where the reactive component is positive (inductive) and can be compensated by a high quality variable capacitor. In both instances the resonant frequency of the coil is adjusted using the tuning variable capacitor C_T, so that Z_0 is equal to 50Ω and the frequency is at ω_0. The tuning capacitor value found by solving Eqn. 2.13

$$C_T\omega_0 = \frac{1}{XC} \tag{2.13}$$

(where $X = 1/\omega C$) and the matching capacitor can be chosen according to Eqn. 2.14

$$C_M = \frac{1}{\omega_0 Z_0 A} \tag{2.14}$$

One should be aware of two possible issues. First, tuning and matching capacitance values will vary as a function of sample loading. Loading generally corresponds to an increase of the resistance value and for that reason the designer should make sure the circuit has a wide tuning and matching range capability to compensate different loading conditions. Second, some of the formulas for component calculation found in RF engineering textbooks (and in this thesis) are meant to give the designer a reference and the order of magnitude of the components value. The RF designer should not expect to use the exact value in the circuit, because most likely the expression used did not take into account all the factors influencing the system.

2.4 Balancing

In Sec. 2.2, when describing noise sources, we presented tissue and radiation losses that originate from the magnetic and electrical interaction of the coil with the sample. Tissue losses are caused by the electric coupling with the sample. The dielectric characteristics of the sample tissue have the effect of decreasing the Q-factor ("de-Quing"), thus decreasing the coil sensitivity. The losses are usually evaluated by comparing the corresponding Q when the coil is loaded against the Q of the unloaded

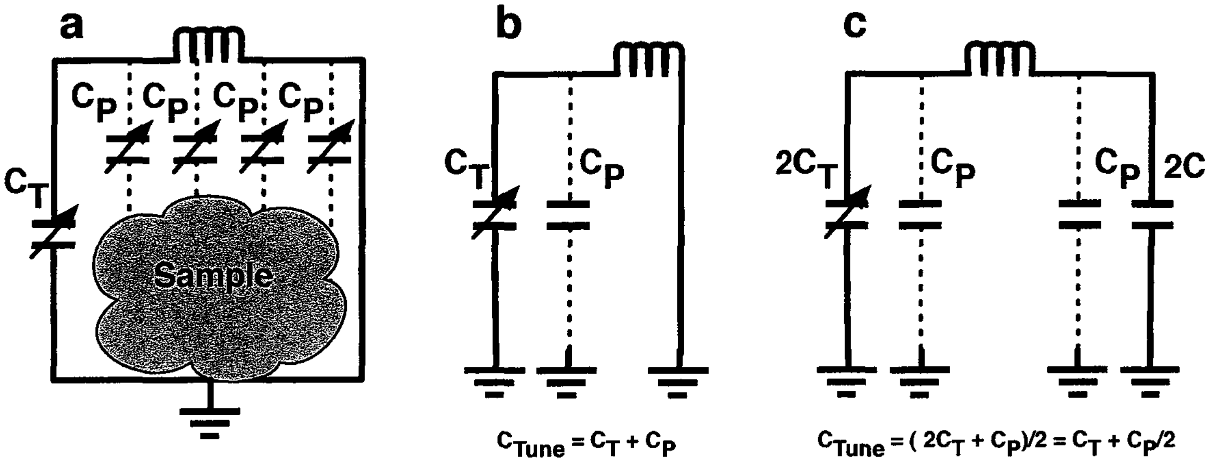

Fig. 2.5: (a) Parasitic capacitance induced by dielectric properties of the sample introduced into the coil electrical circuit. Here is shown, the equivalent impedance matching circuit for non-symmetrical design (b) and symmetrical design (c), with the contribution of parasitic capacitance.

case. These tissue losses, also called dielectric losses, are proportional to the potential difference between the ground and the coil. In such systems, RF current flows through the parasitic capacitors (these are not actual capacitors, the effect relates to the lossy dielectric sample) resulting in dissipation of energy and decrease in the current flowing through lossless tuning capacitors (see Fig. 2.5(b)). To minimize this effect, the electric field amplitude E within the sample, created by varying magnetic fields and voltage differences, should be kept as low as possible. The goal is to reduce the current flowing through the parasitic capacitors and consequently decreasing the corresponding losses. The RF engineer can reduce such effect by selecting a symmetric configuration (see Fig. 2.5(c)), where the tuning capacitor value is doubled as compared to the non-symmetric configuration.

The electromagnetic (EM) radiation losses occur when the coil radiation energy is no longer negligible. In other words, when the coil behaves like a vertical non-directional antenna, energy is lost from an MR perspective [19]: a non-balanced simple coil loop will have a field pattern radiating randomly depending on the phase

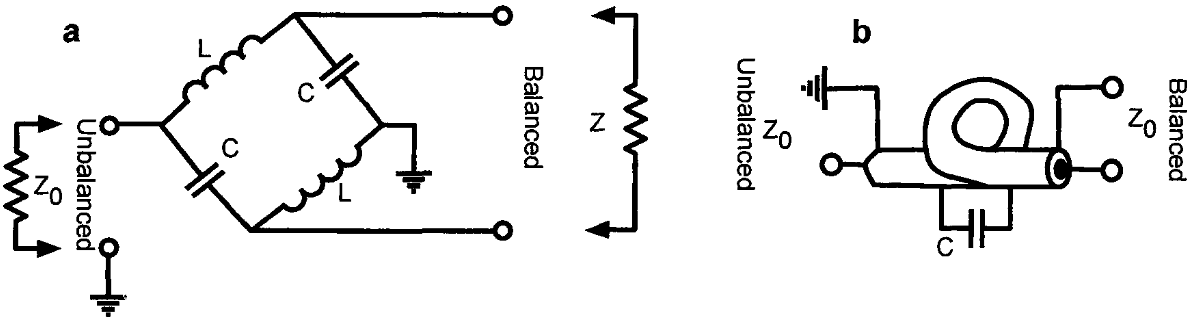

Fig. 2.6: Baluns: (a) LC-balun, (b) trap balun (or "choke"). These are electrical circuits placed in the coil so that floating components are grounded disallowing currents to flow through cable shields, cable conductors or components with different potential. The result is a net zero current.

combination and voltage differences [20]. This problem is avoided by segmenting the actual loop coil: capacitors are inserted in the wire path so that maximum segment length is $\lambda/10$ or less (λ is the system wavelength) [19]. For the segmented coil, the requirement of a symmetrical design still holds. Hence, a balanced segmented coil will have additional Q improvement, over an unbalanced segmented coil loop, a balanced but not segmented coil and significantly higher Q than an unbalanced and not segmented coil.

The voltage differential in the wires and cables connecting to the coil, produces unwanted shield currents flowing to and from the probe. These currents, known as common mode currents, induce additional losses and affect the coil tuning and matching. This effect is commonly known as the "hand effect", as it is easily noticeable by the detuning of the coil when an operator approaches a cable or touches the cable even when coil or cable are shielded. The solution to this problem is to place an electrical device so that currents with opposite phase flow through cable shield and cable conductor, which results in a net zero current on the transmission cables shield. These simple electrical circuits are called baluns, and many different types are used in RF engineering to drive probes in a balanced manner. The LC-balun circuit shown in Fig. 2.6(a), is frequently used in RF coil design because of its unique design that achieves balancing and matching in one stage. The balun is formed by a bridge and the combination of capacitance and inductance can theoretically match any circuits. Unfortunately, depending on the matching required the component values can become unmanageable, which makes the implementation of this design quite complex. Our experience suggested that separating the matching procedure from the balancing using two separate circuits was the appropriate choice. For that reason, in this thesis unless otherwise specified matching is performed with a capacitive network as mentioned above and balancing is achieved using a trap balun, shown in Fig. 2.6(b). The loop formed by the cable is tuned to the frequency of interest via a capacitor. This design, also known as "choke", provides a very efficient way to block braid currents and it is extremely easy to implement.

To summarize, the essential coil design requirement is to obtain the maximum sensitivity and the least power dissipation by following a few simple design rules: lower parasitic capacitance, reduce sample inductive decoupling, break the coil path, and use a symmetric configuration. These principles have been applied to various classic coil designs, which vary according to the intended application, performance characteristic and size of object to image. The next sections will describe the coil designs used to perform the studies in this thesis.

2.5 Volume Coils

As main magnets progressed to higher fields, coil design moved from the linear polarization volume coils, such as the saddle coil [21], multi-turn solenoid [22], to circularly polarized volume coils like the birdcage coil [23, 24] and TEM coil [25]. The latter coils are naturally driven in quadrature mode and therefore ideal for generating B_1 circularly polarized fields (see Sec. 1.2). This type of coil provides lower power requirements and higher SNR (by at most a factor of $\sqrt{2}$), compared to the same coil

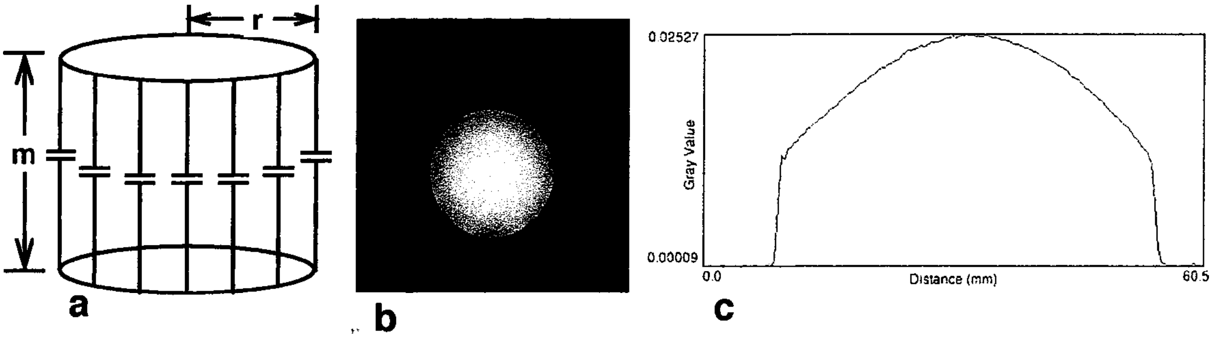

Fig. 2.7: Spatial representation of the birdcage coil, shown in its low-pass version, where the straight segments are known as legs or rungs (a). When the wavelength of the RF field approaches the dimensions of the sample, the standing wave effects may be seen. This effect is demonstrated in the FLASH image (b) and the line plot profile across the center (c) of a spherical (5 cm diameter) copper sulfate phantom with a volume coil at 9.4 T (fd product 25 MHz-m).

driven in linear mode. The birdcage coil design (Fig. 2.7(a)) has significant success, because of its homogeneous field and reliability. This coil, with an ideal current distribution over the cylinder "legs" or "rungs", produces an homogeneous magnetic field in the axial direction. In practical application, the homogeneity improves with increased number of rungs, however increasing the number of rungs also increases construction complexities.

Unfortunately, volume coils like the birdcage coil have significant drawbacks that can negatively affect image acquisition. As the RF wavelength approaches the size of the target object, the RF wave behavior becomes unpredictable, affecting the homogeneity of the B_1 transmit field. Generally, the RF wavelength effect manifests itself as a strong B_1 at the center of the sample and a weak signal at the periphery of the sample [4–6], similarly affecting the corresponding magnitude image (Fig. 2.7(b, c)). If we consider the fd product (a parameter that better describes the relationship between wavelength and sample/coil size), where f is the operating frequency and d is the coil diameter, the RF unwanted effects are dominant, in such cases as human head imaging at 3T and higher, where the fd product is greater than 30 MHz-m, and in small animal imaging (generally in the range of 2-30 MHz-m) the RF wave discrepancies may occur for coils closer to the upper limit of the fd range [26]. The RF effects can be reduced by using multiple surface coils with independent amplitude and phase modulation to tailor the B_1 field.

2.6 Surface coil arrays

The search for an improved solution to RF-related detrimental effects has fueled the already growing interest in transmit surface coil arrays. Multiple surface coils can be used to mimic the transmission and reception operation of volume coils, though with added benefits. By modulating amplitude and phase independently for each coil element during transmission, one can reduce the RF wavelength effects in a process known as "RF shimming" [7, 27]. Also multidimensional RF pulses, created by multiple transmit coils each with its own time-dependent waveform and spatial sensitivity, can be used to implement "Transmit SENSE" [28]. In addition, multiple independent receiver surface coils are required to implement recently introduced parallel imaging (PI) applications [12, 13]. These techniques have become the attractive alternative solution to problems tied with fast imaging acquisition, because of the distinct element sensitivities and higher SNR provided by the phased array at ultra-high fields. In human MRI scanners, there is usually a dedicated coil for transmission and a specific receive coil that changes depending on the body part being imaged. However, in small animal imaging the lack of space inside the bore makes a compelling case for the use of transceive arrays, eliminating the need for the additional transmit body coil. However, despite the many benefits the design of transceive surface coil arrays the design at ultra-high fields poses many challenges.

The primary issue with the design of any phased array or transmit/receive coil is the interaction between elements. Due to mutual inductance, neighboring coils can destructively interact with each other, resulting in resonance splitting of the RF

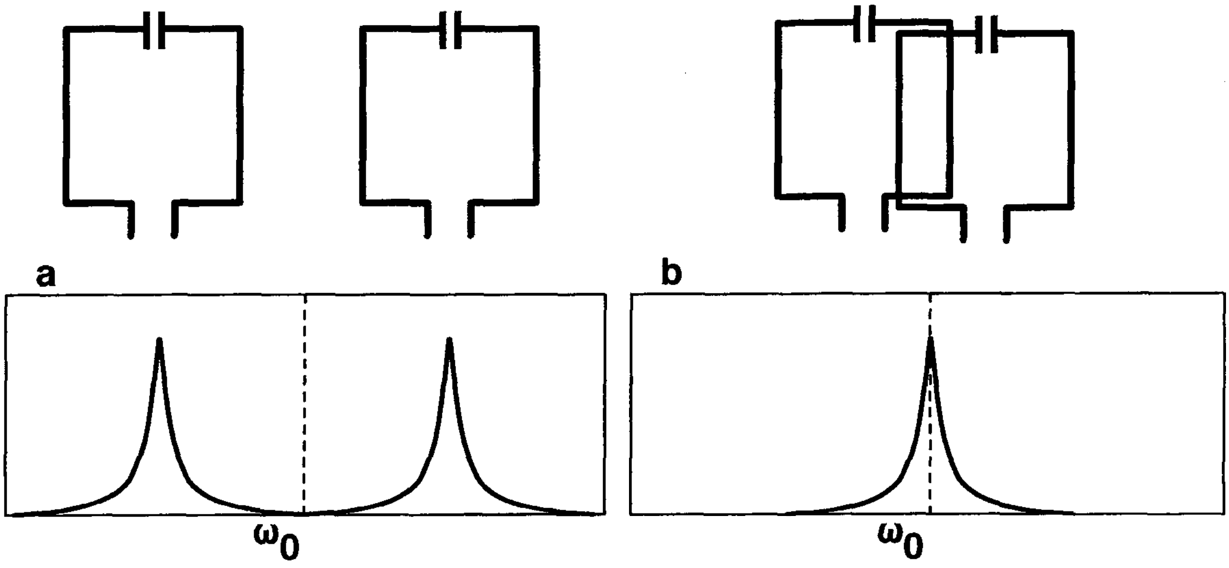

Fig. 2.8: Mutual inductance between two surface coils create a peak splitting effect in the impedance spectrum profile(a). However, when the coil are overlapped (b) the resonator will have one mode behaving like a single coil.

spectrum profile into two modes on either side of the wanted resonant frequency (see Fig. 2.8(a)), which lowers the sensitivity at the original frequency [29]. Decoupling the elements can be achieved in a variety of ways. Preamplifier decoupling [15], a method often used with receive-only systems, becomes less viable due to the fact that low input impedance preamplifiers are not readily available off the shelf. Another decoupling method is used with strip transmission line arrays and their inherent decoupling characteristic [30, 31]. Also, a commonly used decoupling method is achieved by element geometrical overlap [15] (shown in Fig. 2.8(b)). However, this method presents less than an ideal geometry for PI applications where distinct coil sensitivities are required [32]. Finally, complex ladder networks [33] and capacitive networks [29] have been used; however, in recent years other simpler capacitive networks have been devised and shown to be quite successful [4, 34]. The less complex capacitive decoupling method, which was proposed by Wang *et al.* [34], was used in our design to combine multiple surface coils without overlapping and will be described in the next chapter.

Ultimately, the basic element of the phased array, the surface coil, offers high sen-

Ultimately, the basic element of the phased array, the surface coil, offers high sensitivity and high SNR, close to the imaged surface. Higher sensitivity and higher SNR in small individual surface coils is due to the high B_1/I ratio and small effective noise volumes, which translates in higher SNR in phased array coils. In other words the phased array coil "sees" a smaller proton spin density per volume, which means lower tissue noise. The excess SNR can then be used towards accelerating the acquisition with the application of parallel imaging techniques. Therefore despite the complexity in the construction of such coils, there are many advantages that make it worthwhile investigating novel designs for multiple coil transmit/receive arrays.

Chapter 3

Transceive Coil Array: Design And Construction

3.1 Introduction

Generally, in MRI a phased array coil describes a set of receive coils whose signals are combined to obtain a uniform image over a region larger than a single coil of the same size could cover, taking advantage of the high SNR available from the smaller coil. As mentioned in Sec. 2.6, smaller coils have greater SNR as a result of the high B_1/I ratio and smaller effective noise volumes. In our design the phased array is "wrapped" around a cylinder to mimic the operation of a volume coil and the coil elements of the array are used to excite the sample, effectively making our design a transmit/receive (transceive) coil array. The benefits of this design have already been discussed in Ch. 2, however its construction has yet to be covered in this thesis. The main objective in any coil design is to keep all possible noise and power dissipation sources as low as possible; in our design the task was achieved by applying RF engineering principles while implementing stripline segmentation, tuning, matching, decoupling and common mode reduction. In this chapter we will present the construction, testing process of this coil and the results obtained on the

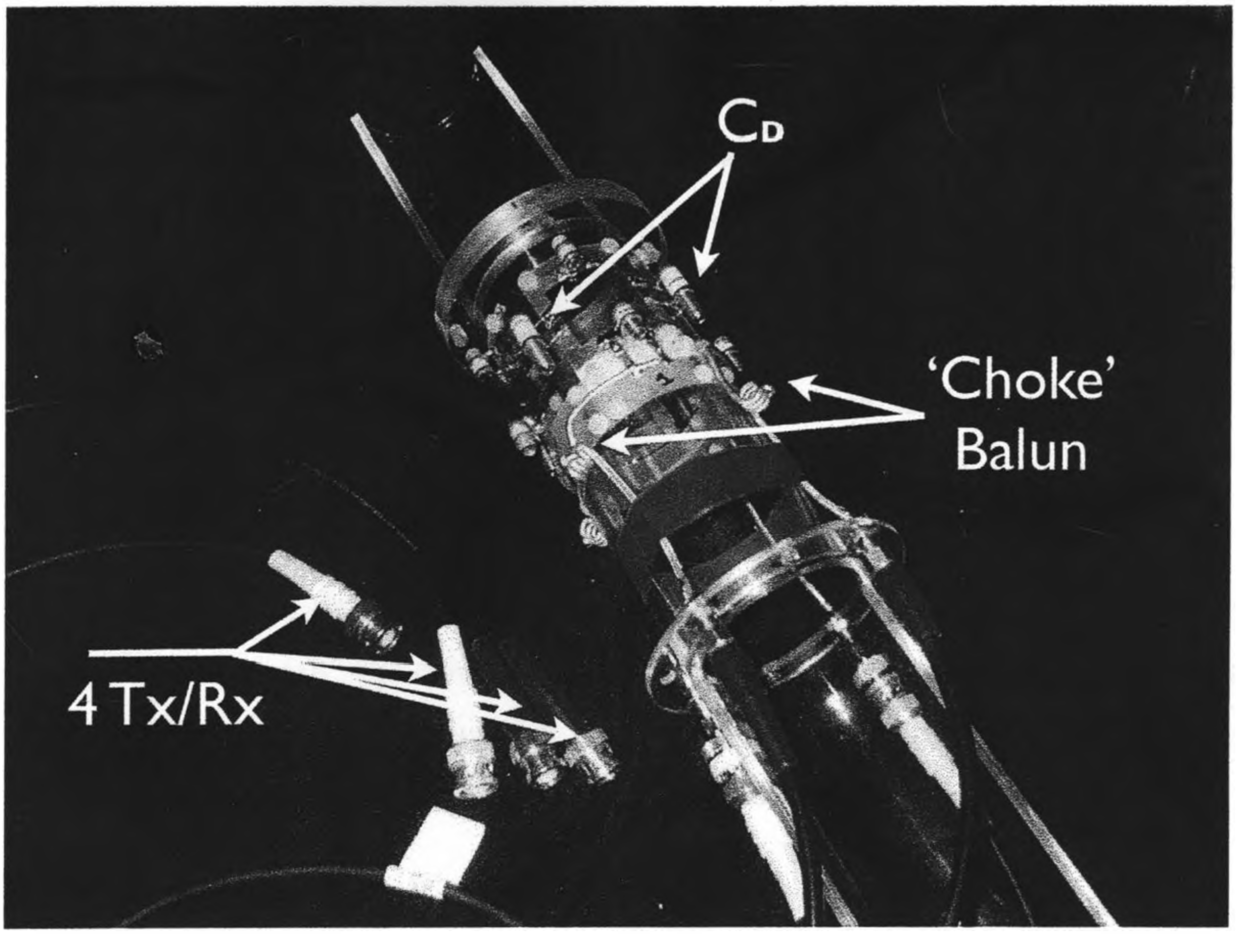

Fig. 3.1: Four-channel transmit/receive (transceive) coil. Four identical surface coil elements are mounted on a cylindrical acrylic former at 0°, 90°, 180° and 270° positions. C_D represents the decoupling capacitor and the choke is also shown, connecting to the each coil port.

workbench.

3.2 Materials and Methods

The surface coil elements were etched from 0.397 mm thick copper clad boards (M.G. Chemicals, Surrey, BC, Canada), into 40 mm per side squares. The thin copper board was used because the element had to be flexible enough to follow the curvature of an acrylic cylindrical former of 63.5 mm diameter, 167 mm length (long axis) and 10 mm thickness. The four elements were mounted on the former at 0°, 90°, 180° and 270° positions (see Fig. 3.1). The former had been shaped to fit into the horizontal bore of a 9.4T animal system MR magnet (Varian, Palo Alto, CA, USA), with the 205/120 HD gradient coil (Varian, Palo Alto, CA, USA). Since only one single transmitter channel was available at the time, a four-way feed network was used (Werlatone, Brewster, NY, USA). Also high precision variable capacitors (Voltronics, Denville, NJ, USA) were used to perform tuning, matching and decoupling.

3.2.1 Radiation Losses

As mentioned in Sec. 2.4, EM radiation losses can be reduced by segmenting the actual coil path with capacitors so that the maximum segment length is $\lambda/10$ or smaller. Considering the formula for wavelength in a dielectric medium, the wavelength in the stripline was calculated using the following:

$$\lambda = \frac{c}{f\sqrt{\epsilon_r}} \tag{3.1}$$

$$\text{Length of segment} \leqslant \frac{\lambda}{10} \tag{3.2}$$

where c is the speed of light, f is the operating frequency and ϵ_r is the relative permittivity of the conductive material. Once the number of segments in the coil loop had been established, we determined the value of the capacitors (to be inserted in the path to break the stripline segmentation).

3.2.2 Capacitor Values Calculation

To calculate the capacitor value for a single element, we recall the equation for the resonant condition

$$f_0 = \frac{1}{2\pi\sqrt{LC_T}} \tag{3.3}$$

where f_0 is 400 MHz (for our system), C_T is the total capacitance, and L is the total inductance that we need to calculate. Although, the inductance for a straight stripline is fairly trivial to calculate, the method we used gives a more accurate value when the geometry of the stripline is not as simple as a finite straight segment. The inductance L was calculated following a few simple steps. First, we arbitrarily selected a value for C for each capacitor (we opted for 10 pF), then we mounted the selected capacitors on the surface element and we measured the resulting resonant frequency, f_1. Second, the total capacitance C_T and f_1 were substituted back into Eqn. 3.3 to find inductance L. Finally, using the actual frequency of operation ($f_0 = 400$ MHz, instead of f_1) and the new found inductance, we recalculated the total capacitance C_T. In our design the inductance is fixed because it depends on the surface area of the copper stripline, which doesn't change; in contrast, the capacitor value may require adjustments once they're inserted in the actual circuit.

3.2.3 Tuning & Matching

The network analyzer was used in two basic display modes to achieve tuning and impedance matching. The first mode (in split screen) displayed the impedance spectrum profile in the primary screen, so we tweaked the tuning/matching capacitors so that the signal peak of the impedance real component was $50\Omega \pm 20$ on the y-axis and 400 MHz on the x-axis. In the secondary screen, the impedance imaginary component had to be concurrently moved as close to 0° as possible (by placing the zero-crossing of the function at 0°). The second display mode showed the reflection coefficient spectrum profile and the goal was to obtain a minimum (the reversed peak) at the resonant frequency in a range of 0 to 100 mV, which is equivalent to perfect null reflection along the 50Ω transmission line. An example showing these results on the display is shown in Sec. 3.3 below. Both spectrum profile modes were also used when analyzing the signal decoupling solution, which we addressed subsequent to the tuning/matching process.

3.2.4 Decoupling Method

Generally, when two coil elements are adjacent, the signal of each element couples with the other. Among the various decoupling methods mentioned in Sec. 2.6, the one we selected is ideal when coil overlapping is not desirable (or not possible) [34]. Usually, when coupling occurs the disruption appears in both element spectrum profiles and can be expressed in term of impedance and the resulting mutual inductance (M):

$$Z_M = R + j\omega M \tag{3.4}$$

where the real part and the imaginary part of Z_M are referred to as resistive and inductive coupling respectively. To reduce the mutual inductance, a capacitor is inserted in the circuit to eliminate the inductance coupling. After inserting the capacitor, Eqn.. 3.4 becomes

$$Z'_M = R + j\omega M + \frac{1}{j\omega C}. \tag{3.5}$$

Therefore, to eliminate the inductive coupling, the imaginary part of Z'_M should be zero or

$$C = \frac{1}{\omega^2 M}. \tag{3.6}$$

Ultimately, the decoupling capacitor can be put anywhere, as long as it is placed along the coil circuit path and its value will depend on the mutual inductance and the distance between the two elements. The decoupling scheme solution was followed by the elimination of common mode currents along the cables [19].

3.2.5 Common Mode Currents

The origin of the common mode effect is explained in Sec. 2.4, and is generally noticeable by the so called "hand effect" that affects coil tuning when an operator

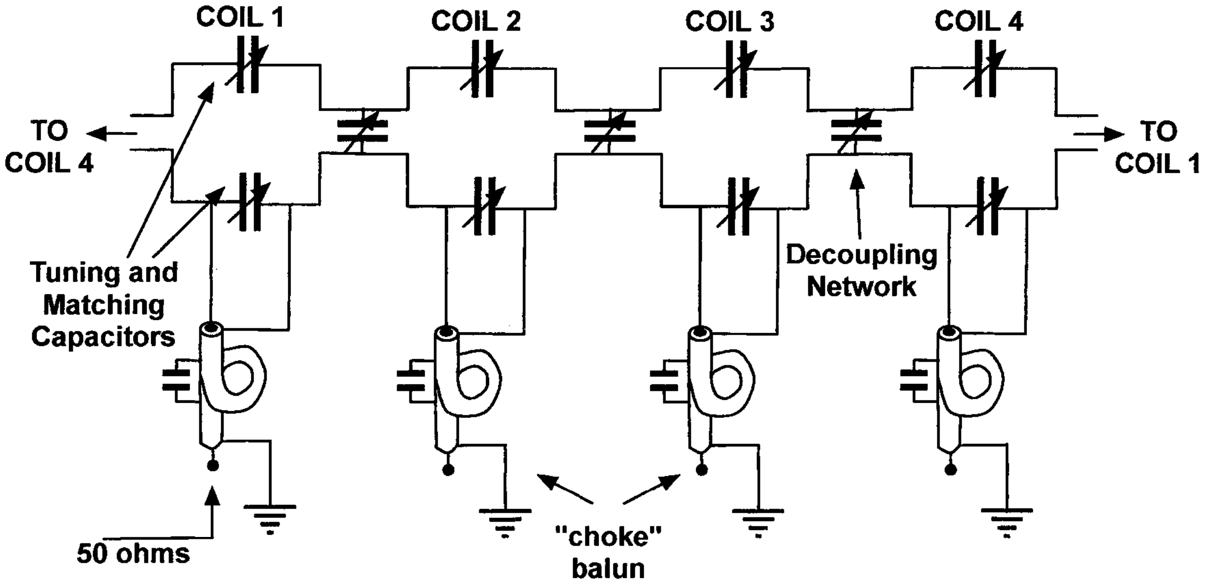

Fig. 3.2: Circuit model for the transceive coil array as shown in Fig. 3.1. The tuning, matching and decoupling variable capacitors are shown. Spatially this circuit is "wrapped" around a cylindrical former.

approaches or touches the cables (even if they have an external dielectric shield). Common mode currents were reduced by inserting choke baluns (see Fig. 2.6(b) or Fig. 3.2) on each line going to an the element. For the choke to be efficient in blocking the currents, it had to be tuned to 400 MHz. So the choke, effectively an LC circuit ((L) inductor and (C) capacitor), was built with a 10 pF capacitor and an inductor constructed winding a flexible braided cable, where adjusting the separation between turns changed the inductance L, and consequently the resonant frequency. The summary of all the elements used is shown in the coil circuit model in Fig. 3.2. After determining tuning/matching ratios, implementing a decoupling scheme solution and adding RF baluns, we were able to test the preliminary performance of the coil by calculating the Q-factor of each element.

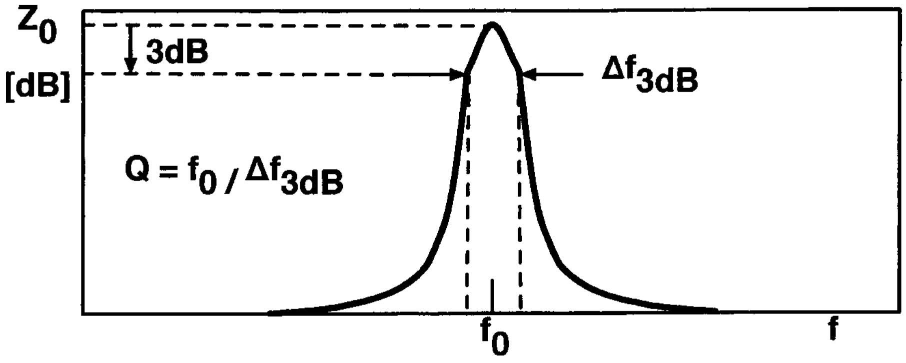

Fig. 3.3: Q-factor calculation. The bandwidth, Δf, of the impedance signal at the resonance frequency is shown on a graph of impedance versus frequency. The Q-factor is calculated at the FWHM (full width at half maximum), which is 3dB in the logarithmic scale.

3.2.6 Q-Factor Calculation

The Q-factor is a unitless parameter that describes the dissipation of energy over a unit time; a higher Q indicates a lower rate of energy dissipation relative to the oscillation frequency, and in electrical engineering it represents a measure of the 'quality' in a tuned circuit or a resonator. In practice, losses in a capacitor (or an inductor) in the circuit, will translate in lower Q. The quality factor Q was calculated according to

$$Q = \frac{f_0}{\Delta f_{3dB}} = \frac{f_0}{BW_{3dB}}, \tag{3.7}$$

where the 3dB bandwidth is directly measured from the RF spectrum response as shown in Fig. 3.3. We performed all of the workbench measurements using an Agilent 4395 Network/Spectrum/Impedance analyzer (Agilent, Santa Clara, CA, USA).

3.3 Results and Discussion

Because a lot of tweaking is involved in most designs, RF engineering practices condone "trial and error" methods, however it's extremely valuable to know the ba-

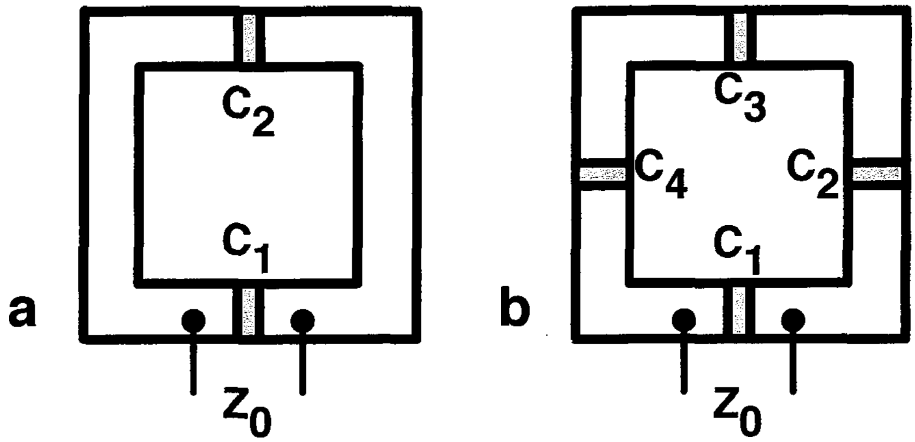

Fig. 3.4: Coil element segmentation. The copper stripline is segmented with chip capacitors to avoid EM radiation losses. In our design segmentation into two striplines (a) does not abide by the $\lambda/10$ requirement, however (b) four segments satisfies that requirement.

sic formulae that regulate component selection: calculating the initial value is vital because knowing the capacitor order of magnitude in advance, facilitates the process and reduces the number of iterations during development.

3.3.1 Component Selection

Using Eqn. 3.1 (ϵ_r=5.4, as per the datasheet) the operating wavelength through the stripline conductor was found to be 322 mm, therefore the segments had to be 32.2 mm or less. If the 40 x 40 mm square surface element was to be split only into two segments (see Fig. 3.4(a)), the length would have been greater than 32.2 mm - not satisfying the required condition, therefore the path was split into four segments as shown in Fig. 3.4(b). It's also important to note that stripline segmentation has another important function (besides decreasing the path to less than $\lambda/10$): it equally distributes the electric field all around the element: a non-uniform electric field would negatively affect the B_1 field produced by each element [35]. The ideal values for the four chip capacitors were calculated and found to be C = 9.3 pF

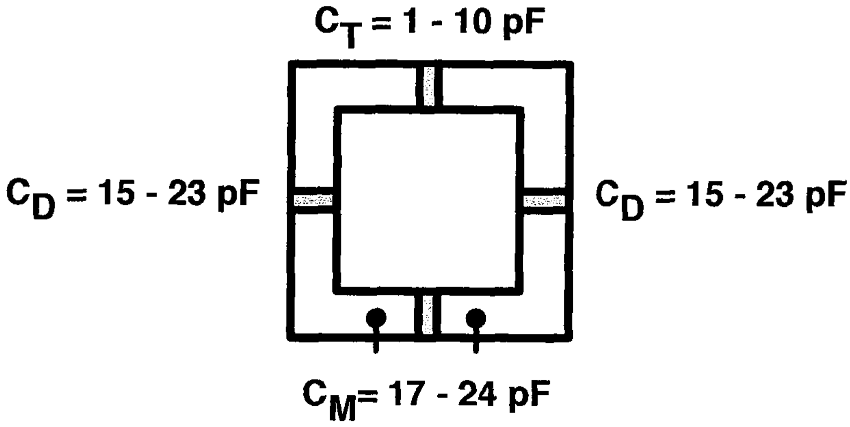

Fig. 3.5: Surface coil element with capacitor values: C_M is the matching capacitor, C_D are the decoupling capacitors and C_T is the tuning capacitor.

and L = 0.136 μH. These were the starting values for tuning and matching capacitors, which were replaced by variable capacitors. Using variable capacitors is important not only because it allows the traditional capacitance tweaking to be performed to match and tune the coil, but also because it can allow a wider tuning/matching range.

3.3.2 Tuning & Matching

In our design, the matching capacitor was chosen to be a 30 pF variable capacitor and the tuning capacitor to be 10 pF variable capacitor (where the capacitor value expresses the max value). For example, with a 5 cm diameter spherical phantom used for some of our experiments, the matching capacitor was approximately 21 pF and the tuning capacitor approximately 3 pF, see Fig. 3.5. The results of the tuning and matching process can be seen in Fig. 3.6; this figure shows the two display modes mentioned above, used throughout our experiment. In human imaging, knees, wrists and other specific body parts are expected to have approximately the same size across average sized adults, therefore usually one body part-specific probe is used. In contrast, the same small animal imaging probe is likely to be used to image a rat or a mouse, a head or spinal cord and other various types of samples. This flexibility is only

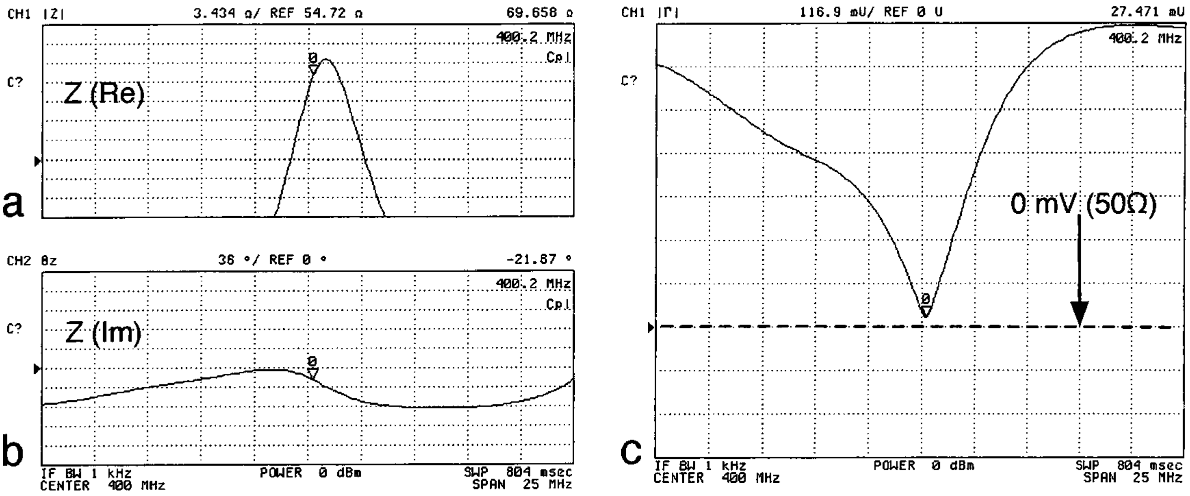

Fig. 3.6: Impedance spectrum profile magnitude (a) and phase (b) of the loaded circuit for the transceive phased array coil. The impedance of the transceive coil is almost purely real (satisfying the resonance condiditon) with a resistance of 69.6 Ω and a small imaginary component represented by the phase at 21.6°. The reflection coefficient shown in (c), is centered at 400.2 MHz, with almost ideal reflection (27.4 mV). Acceptable 50Ω matching is achieved for any value lower than 100 mV.

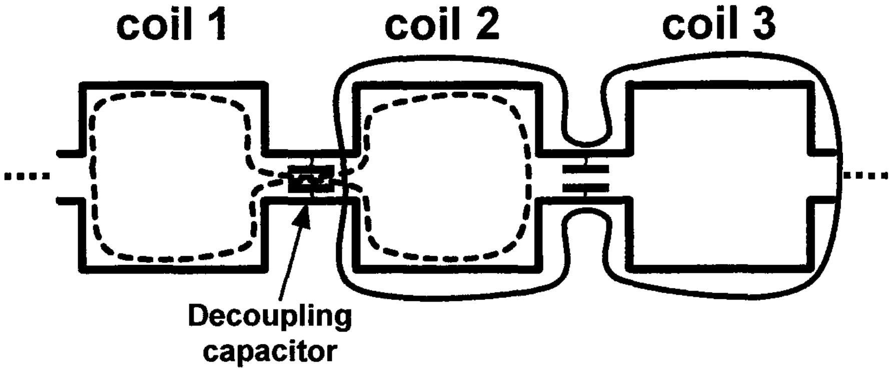

Fig. 3.7: Effect of decoupling capacitor on adjacent coil pair loops: changing the decoupling capacitor value affects "coil 1-coil 2" loop as well as "coil 2-coil 3" loop.

guaranteed by employing variable capacitors, which ensure a greater tuning/matching flexibility. The need of a wide load range for a small animal imaging coil cannot be overemphasized.

3.3.3 Decoupling and Isolation

To solve the signal coupling problem between adjacent elements, we used a systematic approach: we only connected two elements at a time (e.g., coil 1 and coil 2) and found the optimal capacitance that eliminated the peak splitting; we then disconnected that pair, and connected coil 3 to coil 4 and performed the same adjustments. Finally, we connected coil 4 to coil 1 (which are adjacent) and coil 2 to coil 3. It's important to note that because a decoupling capacitor must be inserted in the coil circuit loop and the loops are all connected, that a specific capacitor can influence the tuning and matching of the circuit. For example, the decoupling capacitor between coil 1 and coil 2 has an indirect effect to the decoupling capacitor between coil 2 and 3 (and vice-versa). Therefore, changing the capacitor value affects "coil 1-coil 2" loop as well as "coil 2-coil 3" loop (see Fig. 3.7). Although this process turned out to be tedious and required several iterations, the variable capacitors in the decoupling networks required only that initial adjustment (with a load), thereafter for all the sam-

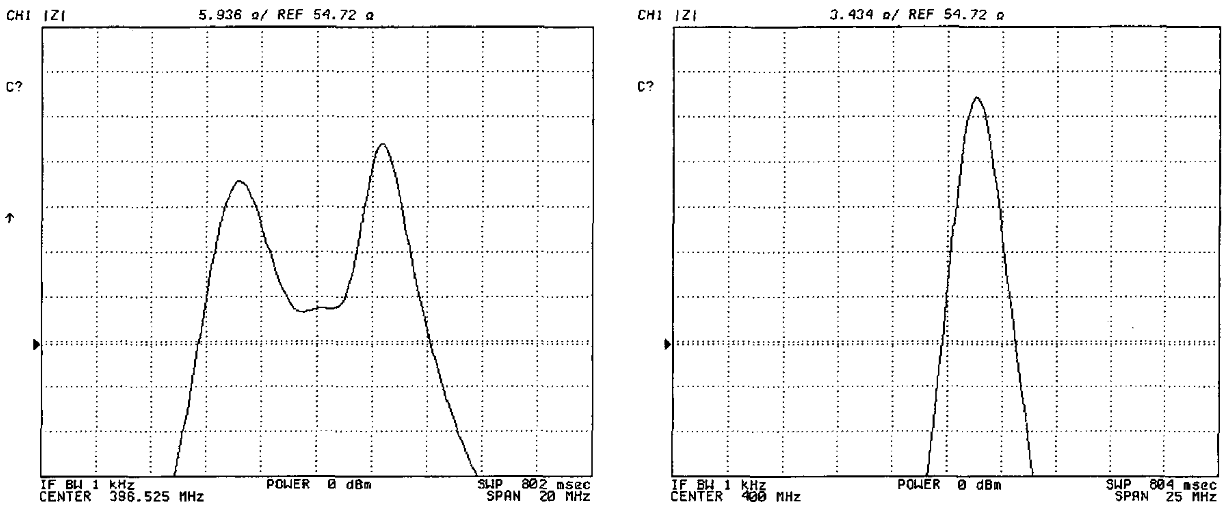

Coupled

Decoupled

Fig. 3.8: Impedance spectrum profile of coil 1 coupled with coil 2 without a decoupling network(left). Impedance spectrum profile of coil 1 decoupled with use of a decoupling network (right).

phantoms, rats), the coil needed only tuning and matching adjustments. An example of the impedance spectrum profile pre-decoupling and post-decoupling is shown in Fig. 3.8. Fundamentally, the capacitive decoupling network enabled each coil to operate as though it were operating in complete isolation. As a result of correct balancing and decoupling, we were able to achieve an average intercoil electric isolation of 12.4 dB (see Tbl. 3.1). For a resonator this size an isolation lower than 10 dB would not be advisable.

3.3.4 Q-factor

Following the isolation measurements, we performed Q-factor measurements to determine the overall quality of each element. The Q-factor is essentially the gain multiplication factor for the MR signal picked up by the coil during reception, as well as the gain for the excitation signal produced during transmission, therefore ideally one would prefer the Q-factor to be the same for all the four elements, in practice

Isolation [dB]	coil 1	coil 2	coil 3	coil 4
coil 1	X	14.2	11.1	10.0
coil 2	14.5	X	13.7	13.3
coil 3	11.3	12.9	X	12.1
coil 4	10.5	13.2	12.3	X

Table 3.1: Intercoil isolation measurements. The isolation is calculated by measuring the impedance spectrum between coil pairs. One coil element is connected to the transmit probe of the network analyzer and the second coil element is connected to the receive probe, the remaining elements are terminated with a 50Ω resistor. Higher isolation values are always preferable and in our design the lowest limit accepted was $\sim$10 dB.

such a result is extremely difficult to obtain. Our workbench measurements of the unloaded Q to loaded Q ratio suggested the system noise was coil dominated (average Q_u/Q_L=1.2 as in Tbl. 3.2) rather than sample dominated. Therefore, it is extremely vital to keep hardware losses as low as possible, and benefit from the low variation of each element sensitivity upon inserting a load (as we further discuss in the next chapter). Finally, although we applied a systematic approach, an ideal improvement to accurately account for each possible source of noise would be to capture them in a modern full-wave 3D electromagnetic software or any other design program that can permit improved coil optimizations. In the absence of such tools the RF engineer needs to be rigorous and methodical in the coil construction.

	Q_U	Q_L	Q_u/Q_L ratio
coil 1	78.5	65.4	1.2
coil 2	74.2	63.1	1.2
coil 3	60.3	53.9	1.1
coil 4	77.9	60.1	1.3

Table 3.2: Q-factor calculations. The 3dB bandwidth of the impedance signal and the corresponding Q-factor was calculated at the resonance frequency, for all four coil elements. This is done with the transceive coil loaded with a spherical phantom and with transceive coil unloaded.

3.4 Conclusions

The technological advances in multiple element MR RF coils of the past two decades have helped fuel the rapid growth in the field of pre-clinical or small-animal MRI. In this regime, the sources of hardware loss due to coil resistance and coil construction in general are important. All such losses may be tackled by following basic RF engineering principles. We were able to reduce noise and power radiation sources by implementing proper stripline segmentation, tuning, matching, decoupling and common mode reduction. Finally, we envision full-wave field simulations and linear-circuit simulations to play an increasingly important role in future advances in MR RF coil technology, especially in phased array where the complex interaction of multiple elements cannot be determined easily.

Chapter 4

Transceive Coil Array: MR Experiments

4.1 Introduction

As previously mentioned, the advancement of multiple coil array design has been considered a viable solution to RF-related detrimental effects [4, 5, 7, 31]. By using multiple surface coils to transmit, the B_1 field can be tailored to reduce standing wave effects. "RF shimming" [7, 27] and "Transmit SENSE" [28] are some example of how the B_1 field can be modified to create custom excitations. In addition, multi-coil arrays can be used for fast imaging acquisitions techniques such as the recently introduced parallel imaging (PI) [12–14].

Both k-space and image based PI techniques, require multi-receiver element coils and their inherent spatial sensitivity information, to unfold the image of an accelerated data acquisition. The major benefit of PI techniques is to reduce scan times, but they can also be used to reduce pulse sequence related artifacts [9, 36, 37]. In single-shot echo planar imaging (EPI), for example, image distortions occur as a result of susceptibility mismatch and off-resonance spin effects. These geometric distortions can effectively be reduced by decreasing interecho spacing [9]. In the same manner multi-shot EPI reduces echo time (TE), the application of PI methods to single-shot EPI can significantly reduce interecho time (and reduce geometric distortion), while maintaining equivalent image resolution. Many examples of PI applied to EPI acquisitions have been presented in human studies [9, 36–38], but the same cannot be said for small animal imaging studies. Only a few publications and conference proceedings exploring small animal imaging coil design for PI in the ultra-high field regime exist [39–42]. Among those, Sutton et al. [40] presented a design that employs two elements as a saddle coil to transmit and four elements to receive, showing that the use of a surface coil array design holds great promise. Nevertheless, designing RF coils for ultra-high frequencies remains a challenge that requires further exploration.

In this chapter, we describe the results of the MR experiments conducted with the transceive coil, specifically addressing the onset of RF wavelength effects. At 9.4T the RF wavelength approaches the size of the sample being imaged [11], therefore the resulting effects cannot be ignored. Furthermore, this design supports parallel imaging reconstruction techniques, which in turn lowers acquisition times and can reduce EPI induced susceptibility artifacts. The results in this chapter, provide an elucidation on the benefits of using transmit/receive (transceive) coil arrays and parallel imaging in animal systems at 9.4T.

4.2 Methods & Theory

We performed all the imaging experiments with a Varian 9.4T Small Bore Horizontal MRI system, 205/120 mm gradient coil and Varian Imaging console (Varian, Palo Alto, CA, US). The transceive coil array as described in Ch. 3 was designed and tuned to operate at 400.2 MHz, with 50Ω impedance. Also, we used a feed-network to split the transmit signal into four equally powered signals, which were incrementally phase shifted by 90° and allowed to drive the coil in quadrature mode. The transceive coil was also compared with an in-house hybrid birdcage coil. The birdcage consisted

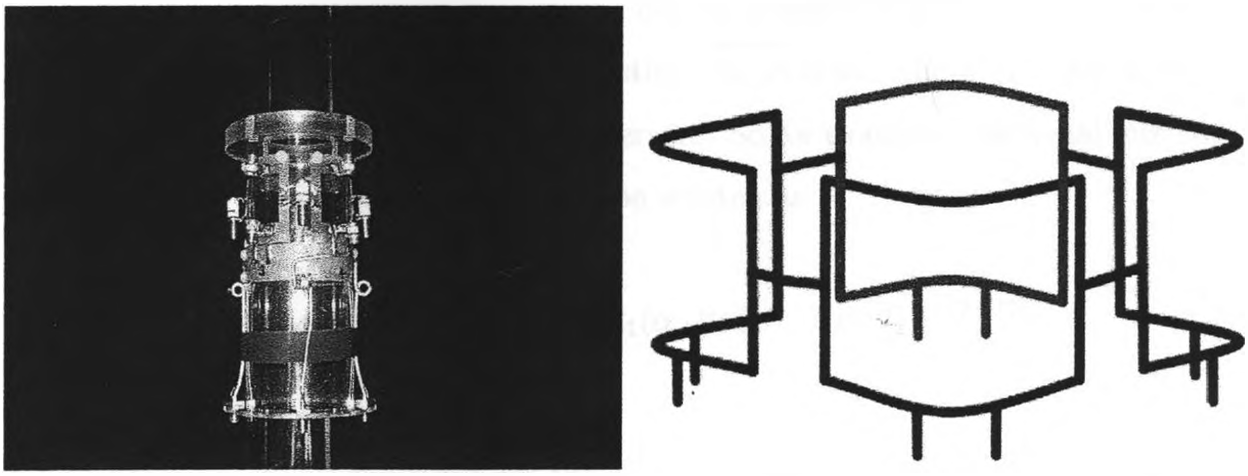

Fig. 4.1: the 4-channel coil array, shown here without the shield (left). The 3-D representation shows the spatial position of the four elements of the coil array (right).

of eight rungs and measured 63.5 mm in diameter (exactly the same as the transceive coil) and 75 mm in length. This birdcage coil was used as a reference system in order to assess the performance of the transceive coil. Although the length of the birdcage was different from the transceive coil, which was constructed with 40 x 40 mm square surface elements, z-axis homogeneity was not our main focus as we performed all the imaging and the comparisons in the axial plane. As mentioned in Sec. 2.5 the fd product is a parameter that relates f, the operating frequency and d, the coil diameter. The RF wavelength effects begin to manifest approximately when the coil fd product is greater than 30 MHz-m, whereas in small animal imaging (generally in the range of 2-30 MHz-m) the dielectric resonance condition may occur for coils closer to the upper limit of the fd range [26].

4.2.1 B$_1$ calculations

Several pulse sequences were used for the acquisition of all the images: 2D fast low angle shot (FLASH), 2D fast spin-echo (FSE), gradient recalled echo (GRE) and echo planar imaging (EPI). The flip angle distribution images were calculated using the double angle method (DAM) [43, 44]. The amount of transverse magnetization induced in the sample by a probe during transmission depends on both the coil characteristics and sample characteristics. In addition, the probe sensitivity is directly proportional to the B_1 that it generates. So for example, the signal intensity estimation I of a spin echo sequence can be written as

$$I = k\,\rho\,S\,\sin^3(\alpha)\,\sin^2\left(\frac{\beta}{2}\right) R_1(\alpha,\,\beta,\,TR,\,TE,\,T_1)e^{-TE/T_2} \tag{4.1}$$

where TR is the repetition time, TE the echo time, α the flip angle of the excitation pulse, β the flip angle of the refocusing pulse, ρ the spin density, k a system constant, S the coil sensitivity and $R_1(\alpha,\,\beta,\,TR,\,TE,\,T_1)$ a general term describing the longitudinal relaxation. The signal is proportional to the several parameters unknown a-priori to the user: the only known parameters are the flip angle and the amount of time that B_1 is applied. Therefore, to eliminate the unknown parameters we calculated the ratio of the signal intensities I_1/I_2 of two spin echo images acquired with identical scan parameters, but different excitation angles α as such

$$\frac{I_1}{I_2} = \frac{\sin^3(\alpha_1)\,R_1(\alpha_1,\,\beta,\,TR,\,TE,\,T_1)}{\sin^3(\alpha_2)\,R_1(\alpha_2,\,\beta,\,TR,\,TE,\,T_1)}. \tag{4.2}$$

The coil sensitivity S, the spin density ρ and T_2 do not change therefore this ratio becomes independent from those parameters. In addition, if we set the repetition time TR to be at least $5T_1$, relaxation terms R_1 cancel out, which leaves us with just the flip angles α_1 and α_2. Finally, setting the condition $\alpha_2 = 2\alpha_1$ allows the determination of the flip angle:

$$\alpha_1 = \arccos\left(\frac{I_2}{8I_1}\right)^{1/3}. \tag{4.3}$$

or

$$B_1^+ = \frac{1}{\gamma\tau} \arccos\left(\frac{I_2}{8I_1}\right)^{1/3}. \tag{4.4}$$

Therefore, the DAM facilitates the determination of the flip angle distribution and consequently the B_1^+ of a loaded RF coil. Additionally, in order to quantify the signal non-uniformities, we calculated a parameter introduced by Wang *et al.* [45]

$$\psi = \frac{\text{SD}}{\text{mean}} \times 100, \tag{4.5}$$

where SD is the standard deviation of the ROI and mean is the average intensity in the same region. Along with the B_1^+ maps, we calculated the SNR in the magnitude images for both the birdcage and transceive coil.

4.2.2 SNR calculations

By definition, SNR is the ratio between the average signal in a small region of interest (ROI), and the root mean square (RMS) amplitude of the noise that is superimposed on the signal. In MR systems the noise has a Gaussian distribution with zero mean, and the RMS amplitude of the Gaussian distribution equals its standard deviation [46]. Therefore, the SNR of a complex image can be measured as the ratio of the average signal (S) to the standard deviation of the noise (σ) measured in a ROI outside the imaged object free from signal, as such:

$$\text{SNR} = \frac{S}{\sigma} \tag{4.6}$$

This is the simple formula holds true for a single-coil acquisition. In contrast, two system-related characteristics make these measurements inadequate for transceive arrays. First, most MR images are presented as magnitude images, rather than complex images, which alters significantly the background noise: the noise distribution is rectified and no longer has a Gaussian distribution nor zero mean. Second, in a sum-of-square reconstruction the statistical distribution of the noise changes, because there is a noise a contribution from each element of the phased array coil, that needs to be taken into account. Therefore, to tackle these issues, SNR calculations in the sum-of-squares magnitude images were performed correcting the statistical distribution of the background noise [47]. We estimated the noise using Constantinides *et al.* ([47], Eqn.[7]):

$$\sigma = \sqrt{\frac{\sum_{i=1}^{L}(\text{pixel value})_i^2}{2Ln}} \tag{4.7}$$

where, L is the total number of pixels and n is the number of coil elements. The SNR for birdcage coil images was measured using the conventional method and corrected taking into account the change from Gaussian distribution, while SNR for transceive coil image was corrected using the method just described.

As mentioned in Sec. 1.3, in parallel imaging signal degradation and SNR reduction occur as a result of increased data sampling rate and increased g-factor as shown by

$$\text{SNR}_{\text{red}} = \frac{\text{SNR}_{\text{full}}}{g\sqrt{R}} \tag{4.8}$$

where the g-factor is not uniform across the image. It reflects an increase in local noise, not a a decrease in signal, which is actually the same for both the non-accelerated and accelerated image. Therefore, in SENSE reconstructed images, we calculated SNR using the 'multiple acquisition' method [46]. Our image stack was comprised of 128 images acquired with identical parameters, and signal and standard deviation were calculated on a per-pixel basis using only the real part of the complex pixel

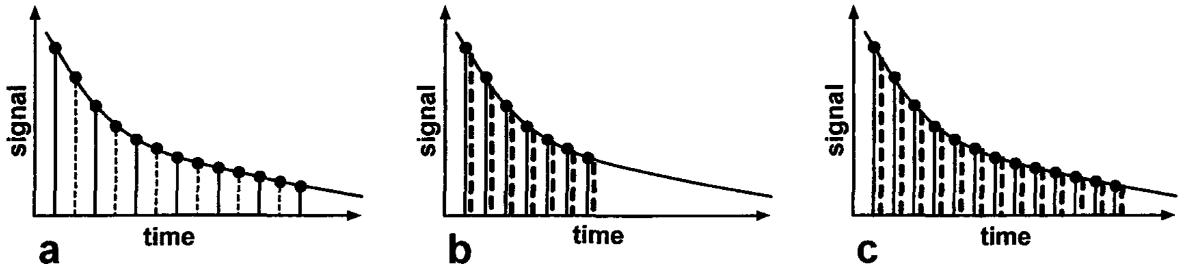

Fig. 4.2: (a) Single-shot signal attenuation representation. The solid black line and the dotted red line represent the acquired odd and even k-space lines respectively. (b) Parallel imaging (PI) strategy 1: the solid black lines are the k-space lines acquired and the red dotted lines are the reconstructed lines via PI techniques. (c) In strategy 2, despite the signal attenuation additional k-space data is acquired further and for a longer amount of time.

to maintain Gaussian distribution. In contrast, measurement of SNR in GRAPPA images (and other k-space based methods) becomes quite complex and is still subject of much debate [46], mainly because the g-factor cannot be quantified.

4.2.3 Parallel imaging reconstruction & applications

We implemented SENSE [13] and GRAPPA [14] reconstruction methods in Matlab. The reference image, required to calculate coil sensitivity maps, was obtained from the square root of the sum-of-squares of all the individual coil images acquired prior to the accelerated data acquisition. The individual coil images were divided by the reference image, then on the resulting raw sensitivity maps we performed smoothing, noise filtering and polynomial fitting. Similarly, auto-calibration lines were acquired before (or after) the accelerated data acquisitions, instead of within the actual acquisition in order to maximize the benefits of a shorter echo train length during single-shot EPI acquisition. Both techniques were used to reconstruct single-shot EPI images and then compared to the fully sampled and multi-shot data. Generally, single-shot images suffer from degraded spatial resolution and geometrical artifacts, as a result of the signal decay and the loss of spatial frequency information repre-

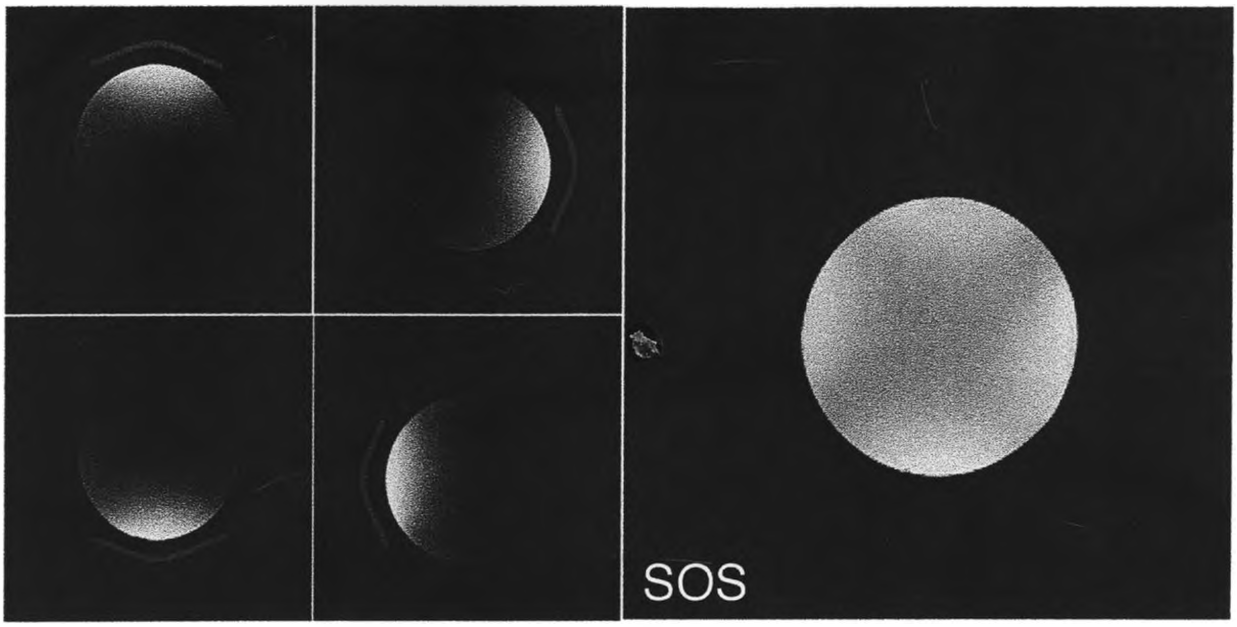

Fig. 4.3: Here are shown the FLASH individual images from each coil element (represented with the red lines). "SoS" is the sum-of-squares combination of the individual images. The parameters are: $FOV_x = FOV_y = 100$ mm , TR =25 ms, TE = 3.5 ms, slice thickness of 2 mm, a tip angle of 11° and 256 x 256 complex.

sented by echoes acquired later in the sequence (see Fig. 4.2(a)). Fortunately, parallel imaging can be used to reduce the echo train length, below the limits of conventional imaging [37]. Specifically, there are two strategies to improve spatial resolution and geometrical artifacts [37]. In the first strategy, PI techniques are used to acquire an image with the same FOV as a fully conventional gradient phase encoded image, but in half of the time or less (Fig. 4.2(b)). The effective echo time (or interecho time) is significantly reduced; consequently, susceptibility and off-resonance related artifacts are also reduced, because the shorter echo train length limits accrual of the phase errors. In the second strategy, PI techniques are used to acquire much more data than it is possible to acquire by conventional methods, increasing spatial resolution when the FOV is left unchanged (see Fig. 4.2(c)).

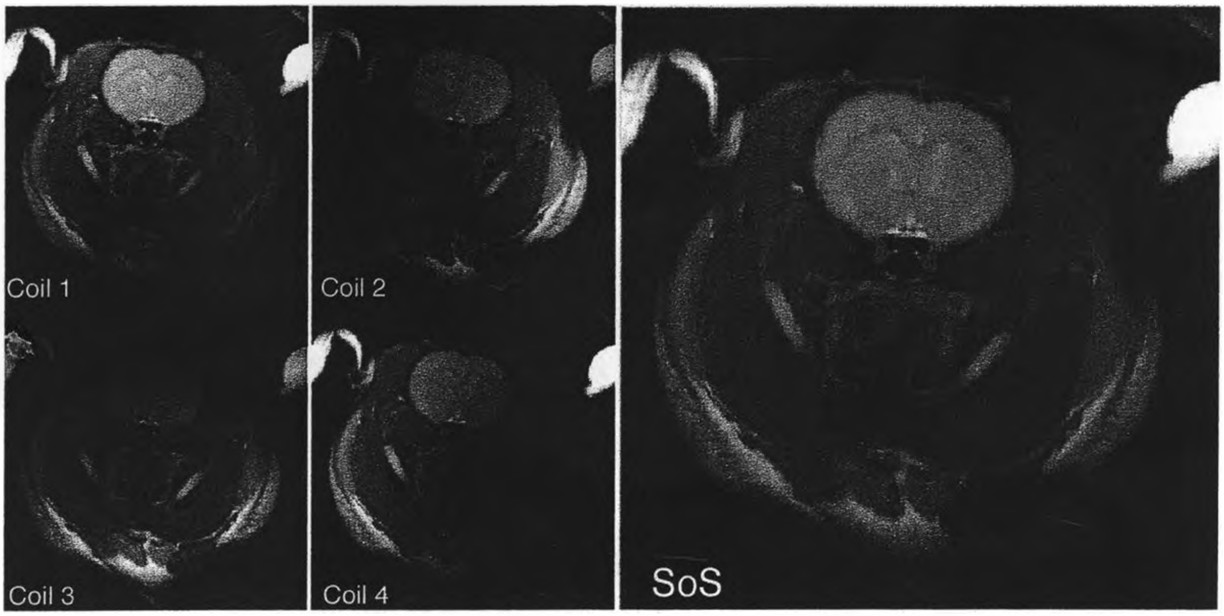

Fig. 4.4: Here are shown the FSE individual images of a rat head from each coil element. "SoS" is the sum-of-squares combination of the individual images. The parameters are: $\text{FOV}_x = \text{FOV}_y = 46$ mm, TR = 5000 ms, TE = 44 ms, slice thickness of 2 mm, a tip angle of 90°, ETL = 8 and 256 x 256 complex points.

4.3 Results

4.3.1 Coil performance: B_1

As mentioned in Sec. 3.3, we performed RF measurements on each element determining that all the coil elements had similar spectrum profiles compared to each other and the transceive coil had an average unloaded Q to loaded Q ratio of 1.2. These results suggested that the coils were properly isolated and the capacitive decoupling networks allowed each surface coil to behave as though it were operating in complete isolation. Most importantly, the decoupling networks required only an initial adjustment (for the loaded case), thereafter all samples (e.g., phantoms, rats), only required adjustment of the tuning and matching capacitors. Fig. 4.3 shows a FLASH image of a copper sulfate filled 5cm-diameter phantom, acquired with the transceive coil (fd product = 25.6 MHz-m): each image acquired from each individual element shows the characteristic intensity of a surface coil acquisition (higher intensity closer

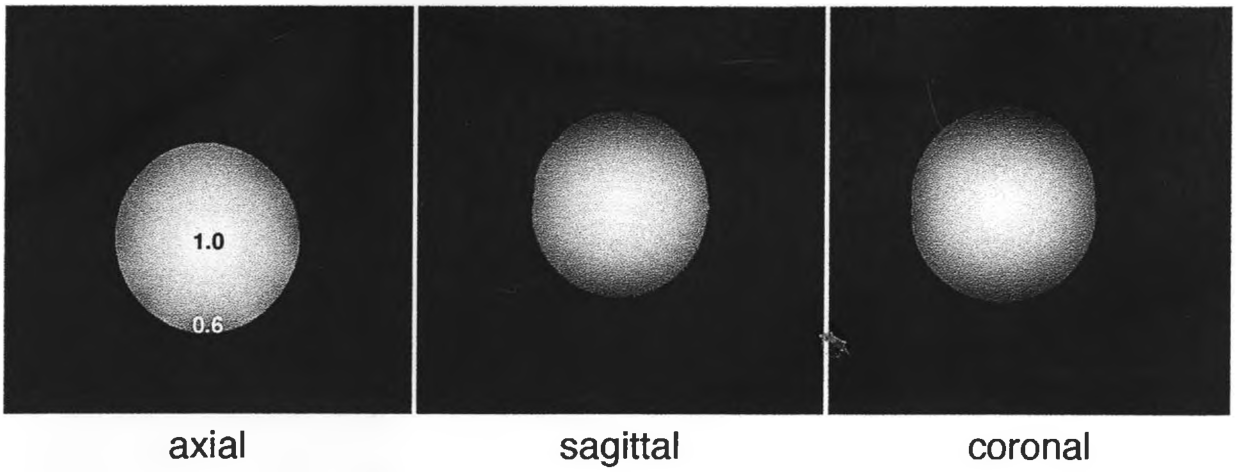

Fig. 4.5: In these slices, acquired with the birdcage coil in the three dimensions, the RF wavelength effect is highly noticeable. The intensity difference between the center and the periphery of the object is almost 50%. The parameters are: FLASH, $\text{FOV}_x = \text{FOV}_y = 100$ mm , TR =25 ms, TE = 3.5 ms, slice thickness of 2 mm, a tip angle of 11° and 256 x 256 complex.

to the element and decaying intensity moving closer to the center of the object). The final sum of square (SoS) reconstruction also confirmed the correct decoupling of each element, since no visible hardware-induced artifacts were present. To further corroborate the phantom results, acquiring data of a rat brain, which had considerably different loading properties compared to the phantom, also resulted in images without artifacts, demonstrating that it was not necessary to adjust the decoupling for a different load, see Fig. 4.4.

FLASH images obtained with the birdcage (fd product = 25.6 MHz-m) highlighted the presence of significant RF wavelength artifacts. In Fig. 4.5 these effects are seen as high intensity in the middle of the image and low intensity at the periphery. As a consequence, we needed to calculate the B_1^+ map fields in both the birdcage coil and the transceive coil, and take advantage of multi-coil array design and its individual controllable elements to reduce or limit RF wavelength effects. Using the spherical phantom, we calculated and compared the transmit field B_1^+ profiles for the transceive and birdcage coil. Fig. 4.6 shows the flip angle distribution α (eqn. 4 [44])

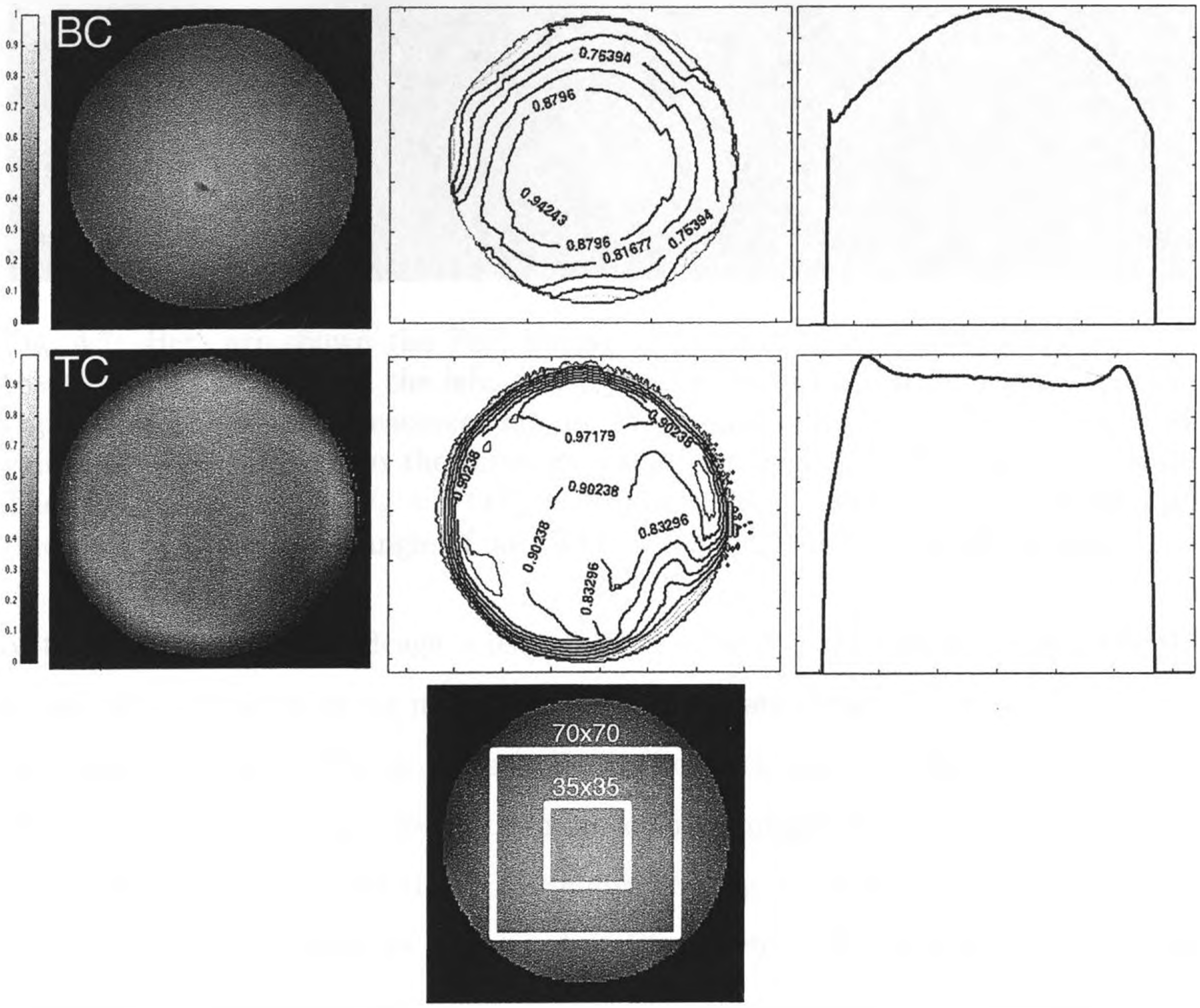

Fig. 4.6: (Left column)The B_1^+ transmit field distribution within a spherical copper sulfate phantom of the high pass birdcage coil (BC) and the transceive coil (TC) are shown. (Middle column) The corresponding contour plots are shown, with the relative homogeneity normalized to the maximum value of B_1^+ transmit field. (Right column) The plot profile of an horizontal line across the center of the phantom is shown. The white boxes at the bottom correspond to the ROIs for inhomogeneity, ψ, calculations. DAM was calculated with two GRE acquisitions with the following parameters: flip angles 60° and 120°, FOV$_x$ = FOV$_y$ = 100 mm , TR = 1500 ms, TE = 5 ms, slice thickness of 2 mm and 256 x 256 complex points.

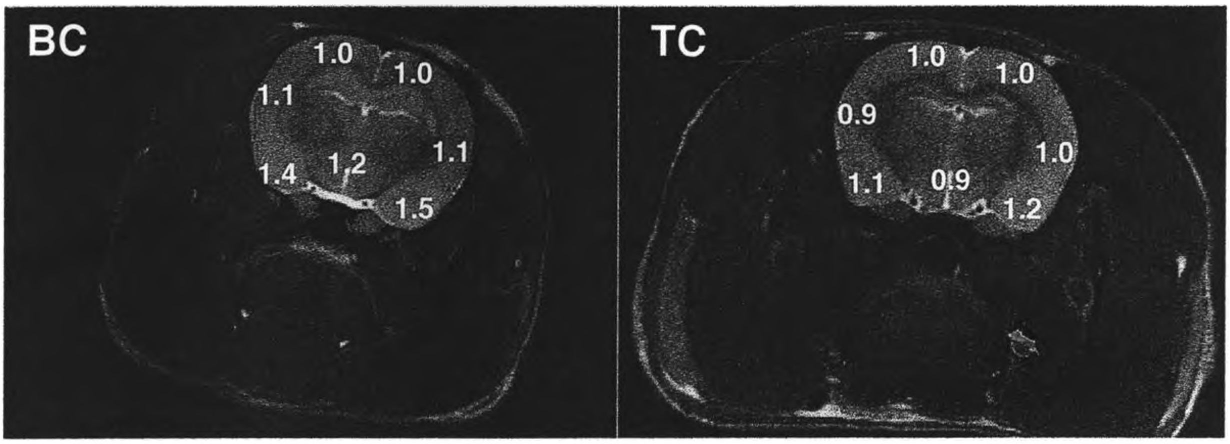

Fig. 4.7: Here are shown the FSE images of two rat brain samples obtained with the birdcage coil (BC) on the left, and transceive coil (TC) on the right. Averaged regional pixel intensity measurements are shown on the images. For each image the values are standardized to the intensity value in a region at the top of the brain. The parameters are: $\text{FOV}_x = \text{FOV}_y = 46$ mm , TR = 5000 ms, TE = 44 ms, slice thickness of 2 mm, a tip angle of 90°, ETL = 8 and 256 x 256 complex points.

of the transceive and birdcage coils, which is directly proportional to B_1^+. For the transceive coil, the transmit magnetic field was adjusted using 10 dB and 3 dB inline attenuators on two of the channels (coil 1 and coil 2), which modified the amplitude of those two channels to effectively improve the homogeneity and symmetry of the signal. We also determined the signal inhomogeneity, ψ, (as proposed by Wang J. *et al.*. eqn. 17 [45]), which we calculated at the center of the phantom (70 x 70 and 35 x 35 pixel ROIs as show in Fig. 4.6). The transmit field inhomogeneity, ψ, was calculated in the large ROI and was found to be 11.06% for the birdcage coil and 8.6% for the transceive coil, and in the small ROI was found to be 7.86% for the birdcage coil and 2.6% for the transceive.

In addition to the in-vitro results, the RF wavelength effects were easily observed in in-vivo magnitude images. Using identical FSE parameters, images of two rat brain samples were acquired with the birdcage coil and the transceive coil. Fig. 4.7 shows these two images and the averaged regional pixel intensity measurements in different areas of the brain. The signal intensity was normalized to the respective top region of the brain.

4.3.2 Coil performance: SNR

Following the B_1^+ correction, we investigated the phantom magnitude images to assess the actual improvement on final magnitude images. Fig. 4.8 compares the FLASH acquisitions prior to inserting the 10 dB and 3 dB inline attenuators. The line plot profiles across the center of the phantom were compared and we calculated the signal discrepancy before the correction and found it to be approximately 35% and 9% (horizontal and vertical profile) at the maximum intensity point. After the correction the deviation was of only 15% and 8% (horizontal and vertical profile). We were also able to record a similar improvement across the center, the profile in the middle-half of the phantom yielded inhomogeneity of 15% and 13% pre-correction and 11% post-correction. These results are summarized in Fig.4.8. Signal intensity uniformity was followed by SNR calculations. SNR comparison between the transceive coil and the birdcage coil yielded an SNR decrease of 42.3% over the center of the phantom and an SNR increase of 51.1% over the peripheral regions. These results were found to be in agreement with those found by Pinkerton et al. [4], where the coil fd product is greater than 30 MHz-m. Ultimately, the lower SNR for the transceive coil at the center of the phantom is expected due to the rapid fall off of the magnetic field B_1 for a surface coil. It's important to note that the higher signal intensity at the center of the phantom observed with the birdcage coil is the result of the RF wavelength effect. Also, we found the mean SNR within the phantom (at least 75% of object ROI) to be comparable between both coils. These results are summarized in Tbl. 4.1.

The in-vivo results agreed almost exactly with the phantom results. The SNR of the rat head images of Fig. 4.7 was measured and found to be 17.2 for the birdcage coil and 10.6 for the transceive coil, corresponding to a factor difference of 1.67. From our previous phantom image results the center SNR ratio, (birdcage to transceive coil)

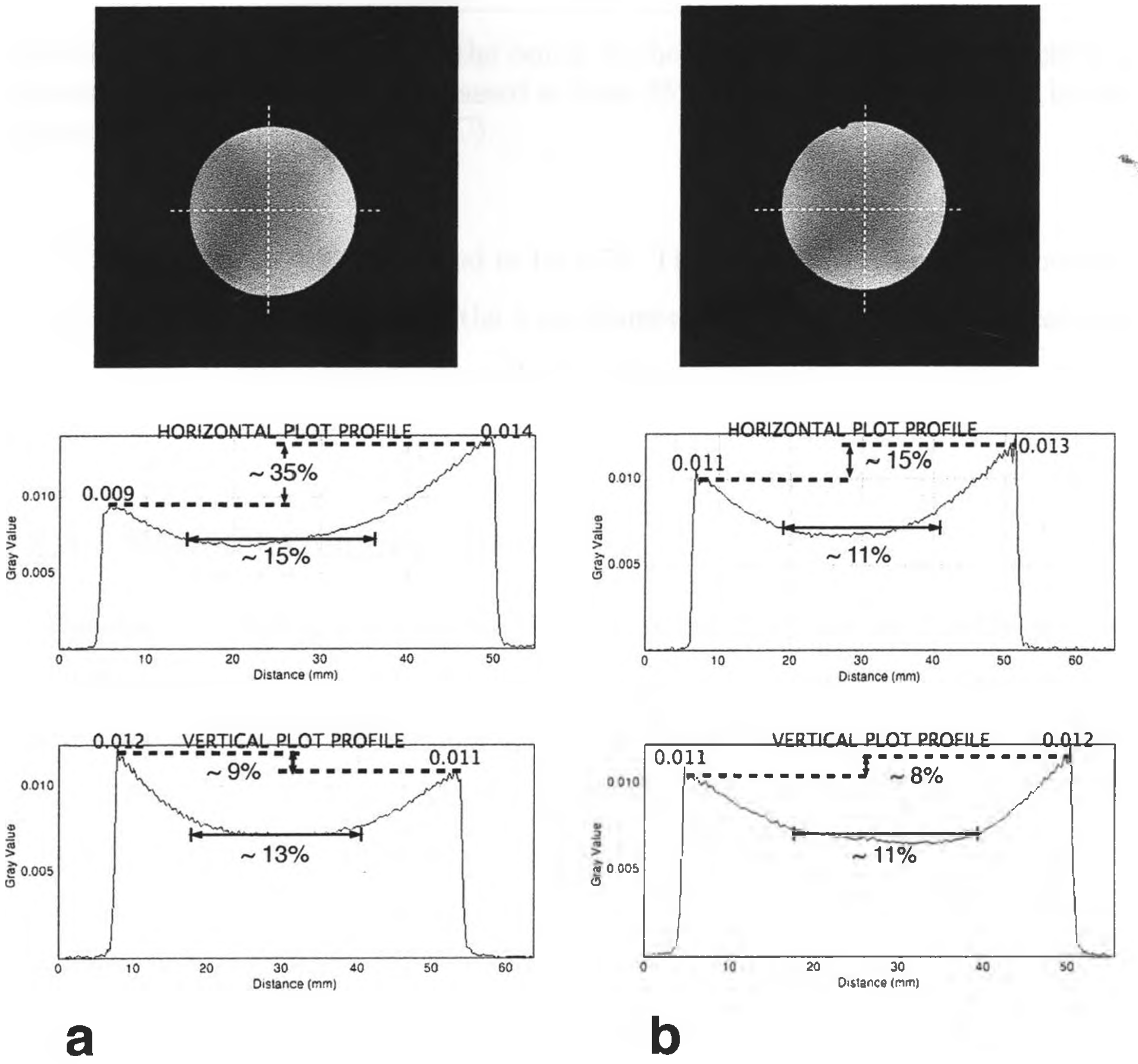

Fig. 4.8: (a) The horizontal and vertical plot profiles across the a spherical phantom are shown here before the B_1^+ correction. Symmetry of the max peripheral point on that line have a discrepancy of 35% and 9%, while across the center 15% and 13%. (b) After readjusting the signal amplitude the discrepancies yielded 15% and 8% (horizontal and vertical profile), and 11% across the center.

	TC	BC
Periphery	276.7	135.4
Center	164.6	285.5
Mean	198.8	219.4

Table 4.1: SNR was compared at the center of the phantom (15 pixel radius circular ROI) and the mean which encompassed at least 75% of the spherical phantom image. Transceive coil (TC), birdcage (BC).

calculated from table 4.1, was found to be 1.73. These results are equivalent because the center SNR ROI calculated in the 5 cm diameter spherical phantom, corresponds approximately to the location where the rat head (of about 2~3 cm diameter) was placed.

4.3.3 Parallel Imaging Results

The ability to distinguish each coil elements sensitivity is essential in the application of PI techniques. As previously mentioned, the benefits of PI lie in the reduction of scan time and also in the reduction of pulse sequence related artifacts. To determine the feasibility of PI methods with our coil, we used SENSE and GRAPPA to reconstruct accelerated EPI data. As shown in Fig. 4.9(a), we acquired a full FOV single-shot EPI with 128 phase encode steps , and using PI methods we were able to acquire and reconstruct the same image with 64 encode steps (Fig. 4.9(c) and Fig. 4.9(d)). These images show significant geometrical distortion reduction, which we were able to achieve by reducing the effective interecho time. The geometrical distortions are defined by the fractional displacement equation

$$\frac{\Delta S}{S} = \Delta f \ * \ T_{intercho} \tag{4.9}$$

where ΔS represents the spatial deviation of the artifacts, $T_{intercho}$ is the interecho time and Δf is the off-resonance frequency. The interecho time reduction attained via PI

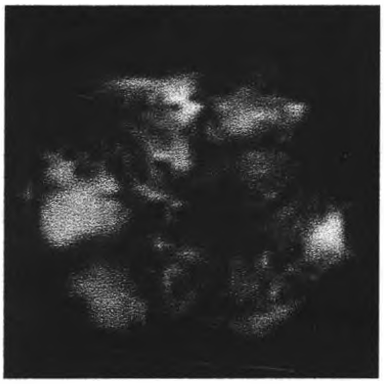

(a) single-shot EPI

(b) 2-shot EPI (c) SENSE, single-shot EPI (d) GRAPPA, single-shot EPI

Fig. 4.9: These images represent the acquisition of cucumber seeds, with the following parameters: ($\mathrm{FOV}_x = \mathrm{FOV}_y = 46$ mm, TE = 18.2 ms, BW = 41.7 KHz, slice thickness = 2 mm). **a**: single-shot EPI: 128 x 128 fully encoded data set **b**: 2-shot EPI: 128 x 64 x 2 shots, fully encoded data set **c**: SENSE recon. single-shot EPI 128 x 64 reconstruction data set **d**: GRAPPA recon (5 ACS lines). single-shot EPI 128 x 64 reconstruction data set. In the single-shot EPI PI reconstructed images (4.9(c) and 4.9(d)), the geometric distortion is reduced when compared to the full FOV single-shot EPI (4.9(a)). The quality of the single-shot EPI PI reconstructed images is comparable to the full FOV 2-shot EPI image (4.9(b))

is comparable to the reduction attainable with a 2-shot EPI conventional acquisition (Fig. 4.9(b)): the geometric artifacts in the PI single-shot acquisitions are reduced as much as in the 2-shot acquisition, when compared with the conventional single-shot acquisition. In addition to the phantom acquisitions, we investigated these results in-vivo. The rat head acquisition presented additional complexities because of the non-uniform physiology of the subject (i.e. varying biological tissue, air cavities), which amplified EPI-induced susceptibility artifacts. This is easily seen in Fig. 4.10(a). The single-shot 64 encoding steps EPI acquisition was then compared to the single-shot 32 encoding steps EPI-PI reconstructed acquisitions. The results show again a sensible improvement in both Fig. 4.10(c) and Fig. 4.10(d). Measurement of SNR yielded the following results. Considering the ideal case, where the g-factor (g) is equal to 1 and the acceleration factor (R) is equal to 2, the expected SNR ratio is 0.707 given by

$$\frac{SNR^{R=2}}{SNR^{R=1}} = \frac{1}{g * \sqrt{R}} \tag{4.10}$$

Our experimental results yielded an SNR ratio of 0.63 which is a decrease of only 10.8% from the ideal case (calculated in signal regions of at least 7x7 pixels).

4.4 Discussion

The benefits of multiple receive coil systems has been extensively established in the literature, initially with the demonstration of SNR improvement [15], and thereafter with time acquisition reduction through spatial encoding with parallel imaging [12, 13]. In recent years, with the increase of magnetic field strength above 4T, it has been also shown that there are additional advantages in using multiple element array coils for RF transmission [4, 7, 28, 31], however such arguments are yet to be widely embraced for the construction of small animal imaging coils. In this chapter we examined the RF wavelength effects and conducted parallel imaging experiments for a multi-element transceive coil.

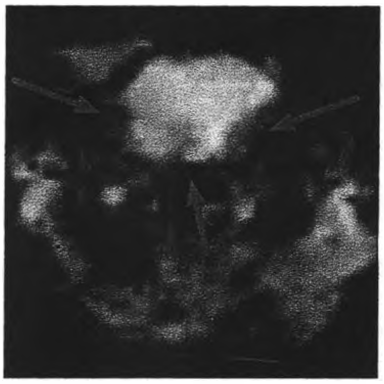

(a) single-shot EPI

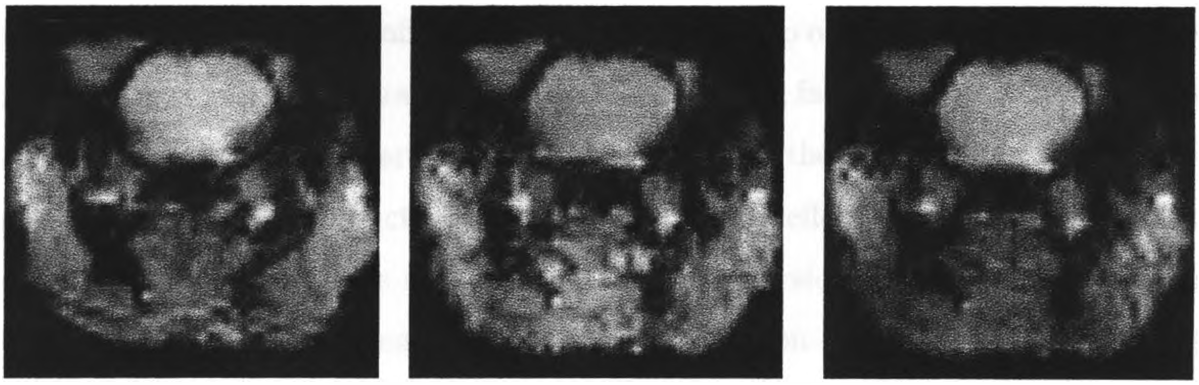

(b) 2-shot EPI (c) SENSE, single-shot EPI (d) GRAPPA, single-shot EPI

Fig. 4.10: These images show the rat head data set: ($FOV_x = FOV_y = 46$ mm, TE = 9.1 ms, BW = 27.7 KHz, slice thickness = 2 mm). **a**: single-shot EPI: 64 x 64 fully encoded data set **b**: 2-shot EPI: 64 x 32 x 2 shots, fully encoded data set **c**: SENSE recon.single-shot EPI 64 x 32 reconstruction data set **d**: GRAPPA recon (5 ACS lines). single-shot EPI 64 x 32 reconstruction data set. In the single-shot EPI PI reconstructed images (4.10(c) and 4.10(d)), the geometric distortion is reduced when compared to the full FOV single-shot EPI (4.10(a)). The quality of the single-shot EPI PI reconstructed images is comparable to the full FOV 2-shot EPI image (4.10(b)).

One of the basic distinctions between a clinical volume coil and a small animal imaging coil, is that the former is usually designed for a specific type of loading in relation to the target body part, whereas the latter usually needs to cover a wider range of loadings. Because the coil we designed had a *low unloaded Q to loaded Q ratio*, the sample load did not heavily impact the performance of the system. This condition can present an advantage in the calculation of sensitivity maps for PI acquisitions. In our design the maps did not significantly change with different loads; therefore, one could potentially use the same maps for different PI acquisitions, thus avoiding the initial reference scan and decreasing the overall scan time.

With the spherical phantom we were able to calculate the B_1^+ distribution and demonstrate the presence of RF wavelength related effects with the birdcage coil, shown as the "bull's eye" profile in Fig. 4.6. The B_1^+ map obtained with the transceive coil initially showed the characteristic surface coil signal fall-off, however we were able to correct the signal by inserting inline attenuators in the transmission lines. Naturally, with a rat head, characterizing the standing wave effect becomes more complex, however in Fig. 4.7 we were able to show that in a physiologically homogenous area of the rat brain, the inhomogeneities of the transmission magnetic signal have a significant effect on the final magnitude image. These results suggest that for a system with fd close to 30 MHz-m as ours was, RF related effects are non-negligible, and further, it demonstrates that there is an advantage in using the surface coil array design for transmission and reception at ultra-high field to reduce those effects. Generally, to eliminate such disruptive RF wavelength effects, it is common practice to independently control the phase of each element, as to obtain the most homogeneous B_1^+ transmit field by minimizing phase cancellations [7]. In that respect, our design could be improved by using an electronic-controlled phase (and amplitude) control for RF tailoring, rather than inline attenuators, which would open interesting possibilities and lay the basis for our future work. As expected the images obtained with the transceive coil had higher SNR at the periphery of the ROI and lower SNR at the center with respect to birdcage coil images. The higher SNR at the periphery can be a benefit for fMRI studies, where higher signal sensitivity may be required in the brain, which can be placed much closer to the coil element for certain animal models.

In general, SNR performance decreases with PI methods, with respect to fully sampled acquisitions. As shown in Eqn. 4.8 the loss in SNR is due to two factors. First, a reduction proportional to the square root of the speedup factor which occurs due to reduced temporal acquisition. Second, the g-factor, which measures the level of noise amplification that occurs as a result of the reconstruction process. The g-factor depends on how distinct the coil sensitivities are at the aliased pixels, which allows to distinguish the signal contribution from each location, and is therefore dependent on the number and configuration of the coils. In general many more coils than the acceleration factor are used to provide a greatly overdetermined system of equations and to improve the numerical condition of the above-mentioned matrix inversion. Also, in SENSE the sensitivity maps are directly calculated, whereas in GRAPPA that information is extrapolated from a few ACS lines, resulting in estimated sensitivity data that are susceptible to accuracy errors. Therefore, we believe that based on our experiment settings our images reconstructed with SENSE have a more accurate reconstruction than the images reconstructed with GRAPPA. In experiments where motion can alter the sensitivity information during the acquisition, GRAPPA can be preferable since the ACS lines can be taken within the actual acquired data; in this case SENSE could have a less accurate sensitivity information and therefore a less accurate reconstruction. Unfortunately, an accurate comparison of the SNR with the two methods is problematic, since g-factor definition in GRAPPA is still the subject of investigation [46]. Finally, additional SNR enhancement could be achieved by improving the g-factor [32, 48]. Optimization of the g-factor by flexible coil element arrangement, could be well suited for our design since it does not implement decoupling by element overlap. SENSE optimization was beyond the scope of this thesis and will be left for future work. With regards to EPI acquisition, the advantage of multi-shot EPI is that it allows for higher resolution images and larger data matrices acquisition at high fields, where the T2* is much shorter compared to low field (1.5T and 3T). The disadvantage however, is that multi-shot acquisition is susceptible to phase discontinuities and motion-induced artifacts between successive k-space readouts, which lead to geometric distortions. To obviate such problems the single-shot acquisition coupled with parallel imaging reconstruction techniques may be used. We showed that with SENSE and GRAPPA EPI acquisition geometric distortions where greatly reduced and comparable to the 2-shot acquisition. It's clear that more research needs to be done to understand how far we can push the limit, and how much can data be undersampled (i.e. R=2, R=3 or maybe R=4), before SNR becomes too low and therefore no longer feasible. Using PI to reduce EPI-induced artifacts is an exciting solution to this known problem in fMRI studies, that requires further investigation and will be tackled in our future work.

4.5 Conclusion

We were able to design and implement a transceive phased array coil suitable for parallel imaging. It was shown that this design is relevant at 9.4T, where the onset of RF wavelength effects is no longer negligible. Also, the space constrictions in the bore of the magnet warrants the exclusion of a body coil, in favor of a transceive coil. The advantages of this design are reaffirmed by the successful implementation of parallel imaging, which can be applied for fMRI studies in small animal imaging.

Chapter 5

Conclusions & Future Work

5.1 Conclusions

The goal and contribution of this thesis can be summarized in its three objectives. First, to build a transmit/receive multi-coil phased array to image small animals at 9.4T: the transmit/receive setup would allow the elimination of an body coil for transmission. Second, to produce a homogenous B_1^+ transmit field, so that RF wavelength effects can be reduced. Finally, to use spatially varying sensitivity information of each element to support parallel imaging reconstruction techniques.

Various coil designs have been used recently to investigate improved solutions for B_1 shimming and parallel imaging [25, 26, 30, 31]. Transmission line arrays, microstrip arrays and TEM coils are just a few examples of designs that have shown great promise. The surface element phased array coil proposed in this thesis has overall comparable performance to the above-mentioned coil designs. It is our opinion that currently there is no clear overall advantage in using one coil over the other, but rather a design should be selected based upon the application and the available resources. It is clear however that the contribution of this thesis lies in the fact that it shows an additional solution to some of the issues experienced with imaging at ultra-high fields. Not only had our interpretation of the solution to ultra-high field issues not been shown at 9.4T, we were also able to provide a practical application, which could be further improved and regularly be employed in fMRI studies.

5.1.1 Design and Construction of a multi-element phased array coil (Ch. 3)

In this chapter we discussed the steps for the design and construction of a multi-coil phased array. The transmit/receive (transceive) coil was built according to basic RF coil design principles. We started from the basic element, which can be described as a simple loop of wire with current flowing through it. This loop can be easily modeled as an RLC circuit, which is an electrical circuit consisting of a resistor (R), an inductor (L), and a capacitor (C) that follows electrical resonant circuit properties. The RF resonator, was tuned to filter out unwanted frequencies, it was also impedance matched to deliver and/or receive the signal with the highest efficiency, with great attention to minimize all possible sources of noise. The tuning and matching was performed by adjusting the variable capacitors on the element. Balancing and decoupling was also implemented to decrease the noise and eliminate inductive decoupling between the adjacent elements. Our results successfully showed that each individual element operated with minimal or no perturbation from the adjacent elements. Isolation values were found to be sufficiently high and Q-factors values were indicative of a system in which coil noise was dominant. The advantage of said system consist of a reduction of adjustments based on different sample loading properties: upon placing different loads only tuning and matching must be adjusted the decoupling is untouched.

5.1.2 Transceive Coil Application for B_1 Tailoring and Parallel Imaging (Ch. 4)

In this chapter, we described the results of the MR experiments conducted with the transceive coil, specifically addressing the onset of RF wavelength effects. At 9.4T the RF wavelength approaches the size to the sample being imaged, therefore images acquired with the birdcage unequivocally display the effects of RF wavelength phenomenon, thus we needed to find a solution to reduce such effects. We were able to demonstrate both in vitro and in vivo that the transceive coil can effectively eliminate RF wavelength effects. Furthermore, it was shown that the transceive design supports the application of parallel imaging reconstruction techniques, which can reduce acquisition times. An interesting application of parallel imaging techniques was the reduction of EPI-induced susceptibility artifacts. The results in this chapter, provided a significant description of the benefits of using transceive coil arrays and parallel imaging in animal systems at 9.4T.

5.2 Future Developments

5.2.1 Investigation and Correction of RF Behaviour

At ultra-high fields the RF behaviour within the human body is quite complex. This phenomenon demands increased studies and developments to provide spatial B_1 phase manipulation to perform RF shimming in order to obtain more homogeneous B_1 in user-defined areas of the human body. In the future our efforts would need to concentrate on techniques for automatic phase calculation and adjustment and amplitude correction through the multi-channel coil.

5.2.2 RF Engineering

Increasing the elements of a phased array coil system, is a research avenue that has gained great momentum. The advantages of such designs are to be found in both transmit and receive operation. In the near future, the new facilities available to our group will demand increased RF development to investigate and quantify the benefits of different multi-coil phased array designs (i.e. surface coils, stripline arrays, transmission line coil, TEM coils).

5.2.3 Parallel Imaging

We've shown one of many possible applications of parallel imaging reconstruction techniques. Increasing the number of elements may facilitate the use of higher reduction factors. However, SENSE optimization should also be investigated in order to gain enough SNR, to reliably increase the reduction factor. It would be a useful experiment to test the limit of this application.

5.2.4 Transmit SENSE

The concept of using parallel imaging to decrease the acquisition time with the simultaneous use of multiple receive coils can be adapted for the parallel transmission of multidimensional RF pulses. A multidimensional RF pulse follows a certain k-space trajectory. Shortening this trajectory shortens the pulse duration. Therefore, the use of multiple transmit coils, each with custom time-dependent waveform and spatial sensitivity, can compensate for the missing parts of the excitation k-space. Shortening multidimensional RF pulses could be an interesting means of making 3D RF pulses feasible even for fast T_2 relaxing species or strong main field inhomogeneities.

5.3 Conclusions

In this thesis it has been shown that technological development has several applications, each with its own scientific merits. The multi-coil phased array was designed for multiple applications and it was easily incorporated into an existing MRI system. It is our belief that RF coil development can closely follow the increasing demands and requirements of ultra-high field imaging.

References

[1] R Pound. Edward Purcell 1912-97, 1997. Physics World.

[2] F Bloch. The Principle of Nuclear Induction. *Science*, 118(3068):425–430, 1953.

[3] PC Lauterbur. Image Formation by Induced Local Interactions: Examples Employing Nuclear Magnetic Resonance. *Nature*, (242):190–191, 1973.

[4] RG Pinkerton, EA Barberi, and RS Menon. Transceive surface coil array for magnetic resonance imaging of the human brain at 4 T. *Magn Reson Med*, 54(2):499–503, 2005.

[5] JT Vaughan, M Garwood, CM Collins, W Liu, L DelaBarre, G Adriany, P Andersen, H Merkle, R Goebel, MB Smith, and K Ugurbil. 7T vs. 4T: RF power, homogeneity, and signal-to-noise comparison in head images. *Magn Reson Med*, 46(1):24–30, 2001.

[6] GH Glover, CE Hayes, NJ Pelc, WA Edelstein, OM Mueller, HR Hart, CJ Hardy, M O'Donnell, and WD Barber. Comparison of linear and circular polarization for magnetic resonance imaging. *J Magn Reson*, 64(2):255–270, 1985.

[7] PF Van de Moortele, C Akgun, G Adriany, S Moeller, J Ritter, CM Collins, MB Smith, JT Vaughan, and K Ugurbil. B(1) destructive interferences and spatial phase patterns at 7 T with a head transceiver array coil. *Magn Reson Med*, 54(6):1503–1518, 2005.

[8] Qing X Yang, Jinghua Wang, Xiaoliang Zhang, Christopher M Collins, Michael B Smith, Haiying Liu, Xiao-Hong Zhu, J Thomas Vaughan, Kamil Ugurbil, and Wei Chen. Analysis of wave behavior in lossy dielectric samples at high field. *Magn Reson Med*, 47(5):982–989, 2002.

[9] RM Heidemann, O Ozsarlak, PM Parizel, J Michiels, B Kiefer, V Jellus, M Muller, F Breuer, M Blaimer, MA Griswold, and PM Jakob. A brief review of parallel magnetic resonance imaging. *Eur Radiol*, 13(10):2323–2337, 2003.

[10] DJ Larkman and RG Nunes. Parallel magnetic resonance imaging. *Phys Med Biol*, 52(7):R15–55, 2007.

[11] F Wiesinger, PF Van de Moortele, G Adriany, N De Zanche, K Ugurbil, and KP Pruessmann. Potential and feasibility of parallel MRI at high field. *NMR Biomed*, 19(3):368–378, 2006.

[12] DK Sodickson and WJ Manning. Simultaneous acquisition of spatial harmonics (SMASH): fast imaging with radiofrequency coil arrays. *Magn Reson Med*, 38(4):591–603, 1997.

[13] KP Pruessmann, M Weiger, MB Scheidegger, and P Boesiger. SENSE: sensitivity encoding for fast MRI. *Magn Reson Med*, 42(5):952–962, 1999.

[14] MA Griswold, PM Jakob, RM Heidemann, M Nittka, V Jellus, J Wang, B Kiefer, and A Haase. Generalized autocalibrating partially parallel acquisitions (GRAPPA). *Magn Reson Med*, 47(6):1202–1210, 2002.

[15] PB Roemer, WA Edelstein, CE Hayes, SP Souza, and OM Mueller. The NMR phased array. *Magn Reson Med*, 16(2):192–225, 1990.

[16] DI Hoult and RE Richards. The signal-to-noise ratio of the nuclear magnetic resonance experiment. *J Magn Reson*, 24(1):71–85, 1976.

[17] FD Doty. Probe Design and Construction. *Encyclopedia of Magnetic Resonance*, 2007.

[18] K Ong, H Wen, AS Chesnick, S Duewell, FA Jaffer, and RS Balaban. Radio frequency shielding of surface coils at 4 Tesla. *JMRI*, 5(6):773–777, 1995.

[19] J Mispelter, M Lupu, and A Briguet. Balancing the probe head. In *NMR Probheads: For Biophysical And Biomedical Experiments. Theoretical Principles and Practical Guidelines*, chapter 4, pages 93–130. World Scientific Publishing, 2006.

[20] G Hall. Monitoring and direction finding. In *The ARRL antenna book*, chapter 39, pages 39–1. Newington, Conn. : American Radio Relay League, 15th edition, 1988.

[21] D. M. Ginsberg and Melvin J. Melchner. Optimum geometry of saddle shaped coils for generating a uniform magnetic field. *Review of Scientific Instruments Review of Scientific Instruments Rev. Sci. Instrum.*, 41(1):122–123, 1970.

[22] Y Li, AG Webb, S Saha, WW Brey, C Zachariah, and AS Edison. Comparison of the performance of round and rectangular wire in small solenoids for high-field NMR. *Magn Reson Chem*, 44(3):255–262, 2006.

[23] CE Hayes, WA Edelstein, JF Schenck, OM Mueller, and Matthew Eash. An efficient, highly homogeneous radiofrequency coil for whole-body nmr imaging at 1.5 T. *Journal of Magnetic Resonance (1969)*, 63(3):622–628, 1985.

[24] J Tropp. The theory of the bird-cage resonator. *Journal of Magnetic Resonance (1969)*, 82(1):51–62, 1989.

[25] P Vernickel, P Roschmann, C Findeklee, KM Ludeke, Ch Leussler, J Overweg, U Katscher, I Grasslin, and K Schunemann. Eight-channel transmit/receive body MRI coil at 3T. *Magn Reson Med*, 58(2):381–389, 2007.

[26] FD Doty, G Entzminger, J Kulkarni, K Pamarthy, and JP Staab. Radio frequency coil technology for small-animal MRI. *NMR Biomed*, 20(3):304–325, 2007.

[27] JT Vaughan, G Adriany, CJ Snyder, J Tian, T Thiel, L Bolinger, H Liu, L DelaBarre, and K Ugurbil. Efficient high-frequency body coil for high-field MRI. *Magn Reson Med*, 52(4):851–859, 2004.

[28] U Katscher, P Bornert, C Leussler, and JS van den Brink. Transmit SENSE. *Magn Reson Med*, 49(1):144–150, 2003.

[29] RF Lee, RO Giaquinto, and CJ Hardy. Coupling and decoupling theory and its application to the MRI phased array. *Magn Reson Med*, 48(1):203–213, 2002.

[30] RF Lee, CR Westgate, RG Weiss, DC Newman, and PA Bottomley. Planar strip array (PSA) for MRI. *Magn Reson Med*, 45(4):673–683, 2001.

[31] G Adriany, PF Van de Moortele, F Wiesinger, S Moeller, JP Strupp, P Andersen, C Snyder, X Zhang, W Chen, KP Pruessmann, P Boesiger, T Vaughan, and K Ugurbil. Transmit and receive transmission line arrays for 7 Tesla parallel imaging. *Magn Reson Med*, 53(2):434–445, 2005.

[32] M Weiger, KP Pruessmann, C Leussler, P Roschmann, and P Boesiger. Specific coil design for SENSE: a six-element cardiac array. *Magn Reson Med*, 45(3):495–504, 2001.

[33] J Jevtic. Ladder network for capacitive decoupling in phased-array coils. *In: Proceedings of the 9th Annual Meeting of ISMRM, Glasgow, Scotland.*, 2001.

[34] J Wang. A novel method to reduce the signal coupling of surface coils for MRI. *In: Proceedings of the 4th Annual Meeting of ISMRM, New York, USA.*, 4:1434, 1996.

[35] J Mispelter, M Lupu, and A Briguet. Heterogeneous resonators. In *NMR Probheads: For Biophysical And Biomedical Experiments. Theoretical Principles and Practical Guidelines*, chapter 9, pages 437–492. World Scientific Publishing, 2006.

[36] R Bammer, SL Keeling, M Augustin, KP Pruessmann, R Wolf, R Stollberger, HP Hartung, and F Fazekas. Improved diffusion-weighted single-shot echo-planar imaging (EPI) in stroke using sensitivity encoding (SENSE). *Magn Reson Med*, 46(3):548–554, 2001.

[37] MA Griswold, PM Jakob, Q Chen, JW Goldfarb, WJ Manning, RR Edelman, and DK Sodickson. Resolution enhancement in single-shot imaging using simultaneous acquisition of spatial harmonics (SMASH). *Magn Reson Med*, 41(6):1236–1245, 1999.

[38] JA de Zwart, PJ Ledden, P Kellman, P van Gelderen, and JH Duyn. Design of a SENSE-optimized high-sensitivity MRI receive coil for brain imaging. *Magn Reson Med*, 47(6):1218–1227, 2002.

[39] X Zhang and A Webb. Design of a capacitively decoupled transmit/receive NMR phased array for high field microscopy at 14.1T. *J Magn Reson*, 170(1):149–155, 2004.

[40] BP Sutton, L Ciobanu, X Zhang, and A Webb. Parallel imaging for NMR microscopy at 14.1 Tesla. *Magn Reson Med*, 54(1):9–13, 2005.

[41] D Gareis, T Wichmann, T Lanz, G Melkus, M Horn, and PM Jakob. Mouse MRI using phased-array coils. *NMR Biomed*, 20(3):326–334, 2007.

[42] P Ullmann, S Junge, F Hennel, A Nauerth, I Panagiotelis, W Ruhm, and J Henning. High field parallel imaging in rats. *In: Proceedings of the 11th Annual Meeting of ISMRM, Kyoto, Japan.*, page p. 1610, 2004.

[43] EK Insko and L Bolinger. Mapping of the radiofrequency field. *J Magn Reson, Series A*, 103(1):82 – 85, 1993.

[44] R Stollberger and P Wach. Imaging of the active B1 field in vivo. *Magn Reson Med*, 35(2):246–251, 1996.

[45] J Wang, M Qiu, QX Yang, MB Smith, and RT Constable. Measurement and correction of transmitter and receiver induced nonuniformities in vivo. *Magn Reson Med*, 53(2):408–417, 2005.

[46] S Reeder. Measurement of signal-to-noise ratio and parallel imaging. In *Parallel Imaging in Clinical MR Applications*, pages 49–61. Springer Berlin Heidelberg, 2007.

[47] CD Constantinides, E Atalar, and ER McVeigh. Signal-to-noise measurements in magnitude images from NMR phased arrays. *Magn Reson Med*, 38(5):852–857, 1997.

[48] JA de Zwart, P van Gelderen, P Kellman, and JH Duyn. Application of sensitivity-encoded echo-planar imaging for blood oxygen level-dependent functional brain imaging. *Magn Reson Med*, 48(6):1011–1020, 2002.